A displacement formulation for coupled elastoacoustic problems that preserves flow irrotationality

Jie Deng, Oriol Guasch, Laurent Maxit

A displacement formulation for coupled elastoacoustic problems that preserves flow irrotationality

Jie Deng[a,b,*], Oriol Guasch[b], Laurent Maxit[c]

[a] *Chongqing Industry Polytechnic College, 401120 Chongqing, China*
[b] *Human-Environment Research (HER) group, Department of Engineering, La Salle, Universitat Ramon Llull C/Quatre Camins 30, 08022 Barcelona, Catalonia, Spain*
[c] *INSA–Lyon, Laboratoire Vibrations-Acoustique (LVA) 25 bis, av. Jean Capelle, F-69621 Villeurbanne Cedex, France*

Abstract

Two-way fluid-structure interaction (FSI) problems, in the sense that a flow induces the motion of a solid, which in turn modifies the flow boundary conditions, have been approached with very different strategies, the most common of which is probably the finite element method (FEM). In the case of elastoacoustics, the flow consists of an acoustic field interacting with a vibrating structure. When the problem is discretized with the FEM, an algebraic block matrix system is obtained and the coupling between the acoustic field and the structure takes place through a coupling matrix with off-diagonal terms. Usually the structure is characterized by its displacement field, while for the acoustics several options are available, ranging from pressure to acoustic displacement or velocity/displacement acoustic potentials. Depending on the formulation, symmetric or asymmetric systems are obtained and different types of numerical stability problems have to be faced. In this work, a monolithic strategy based on the Rayleigh-Ritz method is proposed. The displacement is used as the primary variable for both the structure and the acoustic field and is expanded in terms of Gaussians as basis functions. This provides an algebraic block matrix system for the global uncoupled problem. However, instead of resorting to a coupling matrix, the essential continuity conditions at the acoustic-structure interface are imposed by the nullspace method (NSM). That is, the solution of the uncoupled system is expanded in terms of a basis of the nullspace generated by the essential conditions of the problem, including the displacement continuity constraints at the interface, thus giving the solution of the coupled problem. As for natural conditions, they are imposed in a weak sense. For ease of explanation, a one-dimensional (1D) case is first introduced, followed by the coupling of a 2D acoustic cavity with a beam and a 3D one with a plate. The proposed method is validated with FEM simulations on fine meshes and the advantage of using Gaussian basis functions over trigonometric ones is also demonstrated.

Keywords: Fluid-structure interaction, Vibroacoustics, Elastoacoustics, Displacement continuity, Nullspace method

1. Introduction

Fluid-structure interaction in vibroacoustics involves the interaction of an acoustic field with a vibrating structure. In the two-way problem, the acoustic waves induce vibrations in the structure, which in turn modify the acoustic field. In the one-way problem, a vibrating structure radiates acoustic waves with negligible feedback from them. In this paper we consider the two-way elastoacoustic problem, where an elastic body interacts with the acoustic field in a cavity, in the low-mid frequency domain, where deterministic models are applied. Therefore, statistical methods for the high frequency range, such as statistical energy analysis [1] and related methods, are not considered.

*Corresponding Author: jie.deng@salle.url.edu

The two-way elastoacoustic problem at low and medium frequencies has important applications in industry and has been studied for decades using several analytical and numerical methods, like the finite element method (FEM) or the boundary element method (BEM) (see e.g., [2–6] for initial works and [7, 8] for more recent reviews). Because of its versatility, FEM is probably the most widely spread approach, but it is not free of numerical difficulties. While displacement is the natural variable to characterize the structure, there are different options for the fluid, namely the acoustic pressure [9, 10], the velocity potential [11, 12], the displacement potential [13, 14] or the acoustic particle displacement [15–17]. The latter option has the advantage over the pressure and displacement potential formulations that it leads to symmetric discrete systems and facilitates the imposition of boundary conditions at the interface. However, it was soon realized that the displacement/acoustic displacement approach had some problems, as spurious circulation modes without physical meaning appear for the standard Galerkin FEM. These spurious modes could be partially eliminated by imposing an irrotationality constraint using a penalty method [2, 16, 17] and are associated with the fact that the problem admits a zero eigenvalue whose corresponding eigenspace is that of pure rotational modes. When the problem is discretized with the FEM, the zero eigenvalue is split into several non-zero eigenvalues, thus polluting the spectrum, since non-zero eigenvalues correspond to irrotational modes [18]. To remedy this issue, it was proposed in [18, 19] to use different FEM spaces for the structure and the fluid. In particular, standard triangles/tetrahedra were used for the structural displacement and Raviart-Thomas elements for the fluid displacement. The interface requires special treatment to match the meshes and an additional pressure variable is used to impose the continuity conditions in a weak sense [20]. Subsequently, it was shown in [21] that the displacement/velocity potential formulation was equivalent to the displacement/acoustic displacement approach in [20], thus inheriting its numerical performance. More recently, significant progress has been achieved using non-conformal FEM spaces in the framework of the discontinuous Galerkin method [22–24].

As for the Rayleigh-Ritz method, it has recently been used for the two-way problem using velocity/pressure formulations and trigonometric basis functions [25–27], and has been widely exploited for the one-way problem of calculating sound waves generated by vibrating surfaces using different sets of test functions. For instance, polynomials were used for the radiation of unbaffled plates and beams in [28–30] as well as trigonometric functions for baffled [31–34] and unbaffled plates in [35]. More recently, Daubechies wavelet functions have also been applied for the one-way problem of plate radiation with embedded acoustic black holes [36–38] and in [39–43] Gaussian functions were used instead for different types of acoustic black hole plates and metaplates.

In this work, it is proposed to solve the two-way elastoacoustic problem using a displacement/acoustic displacement formulation and Gaussians as basis functions in the framework of the Rayleigh-Ritz method. From the Euler-Lagrange equations we derive the uncoupled equations of motion of the system in the form of an algebraic block matrix system without cross matrices. While in the above-mentioned FEM and Rayleigh-Ritz works coupling takes place through off-diagonal terms in the mass and stiffness block matrices of the discrete system, which could be combined into a coupling matrix, we propose to prescribe the continuity conditions at the interface in a very different way. In particular, while traction continuity is imposed in a weak sense, we will resort to the nullspace method (NSM) [44] to strongly impose displacement continuity. The NSM has proven very efficient in characterizing structure/structure [45], and fluid/fluid interactions [46] (see also [47, 48]). The key idea of the NSM is to expand the solution of the uncoupled problem in terms of the basis of the nullspace generated by the displacement continuity conditions at the structure-fluid interface and other essential boundary conditions of the problem. In this way, the solution of the coupled problem can be obtained. For ease of explanation, the proposed approach is first presented for a one-dimensional (1D) problem consisting of acoustic waves driven by a piston resonator. Then, the cases of two enclosed cavities separated by a structural element are considered in 2D and 3D. The validity of the method is assessed by comparison with FEM simulations on fine meshes.

Finally, it is worth mentioning that the two-way elastoacoustic problem addressed in this work can be treated without assuming great simplifications due to its relatively small dimensions. However, in industry it is common to face vibroacoustic problems in very large structures. In such situations it becomes mandatory to resort to substructuring approaches and to assume simplified conditions at the fluid-structure interface. In this sense, the essentials of the component mode synthesis (CMS) were set in the classical papers [49–53] and

have been well developed for numerical methods involving some type of mesh [54–57]. Only very recently the CMS was extended in the Rayleigh-Ritz context [58]. Alternatively, the dual modal formulation for linking components with very different impedance mismatch, such as those in weak fluid-structure interactions, was established in [59–61]; see also its extension to higher frequencies [62–64] and to multiple connected subsystems with strong [65] and low [66] impedance mismatch. Another widely used method for large vibroacoustic problems is the patch transfer function method [67].

The paper is structured as follows. For simplicity, we start by formulating the 1D problem in Section 2 and derive the equations of motion for the uncoupled and coupled cases using the NSM. A validation with the FEM is included. In Section 3, we consider a 2D problem consisting of two closed acoustic cavities separated by a beam and show how the proposed methodology can be applied in this more complex scenario. An extension to 3D cavities separated by a plate follows in Section 4. The coupled and uncoupled modes of the system are presented. Special emphasis is placed on showing how the irrotational nature of the flow is preserved and how the acoustic pressure field can be recovered from the displacement field. Conclusions close the paper in Section 5.

2. One-dimensional (1D) problem: plane waves in a duct coupled to a resonator

2.1. 1D problem description

To better illustrate the proposed method, we first consider a 1D model in harmonic regime, consisting of acoustic plane waves propagating in a rigid duct that is coupled with a resonator (piston) at its right end, see Fig. 1. The duct has length $L = 0.8$ m and diameter $h = 0.01$ m, and is filled with air of density $\rho_0 = 1.21$ kg/m^3 and speed of sound $c_0 = 343$ m/s, or water with $\rho_0 = 1000$ kg/m^3 and $c_0 = 1500$ m/s. The piston at the right end has mass $m = 0.01$ kg, and is connected to the ground by a spring of stiffness $k = m\omega_r^2$, where $\omega_r = 2\pi f_r$ and $f_r = 50$ Hz is the eigenfrequency of the resonator.

2.2. Lagrangian of the 1D system

Let us begin by presenting the Lagrangian of the fluid inside the duct, which is obtained by subtracting the potential energy, U_a, from the kinetic energy, T_a, of the acoustic field, and adding the work done by the resonator (piston) on the fluid, W_{ra}. The kinetic energy is given by $T_a = (1/2)\int_0^L \rho_0 h v^2 \mathrm{d}x$, where v is the acoustic particle velocity, while the potential energy is given by $U_a = (1/2\rho_0 c_0^2)h\int_0^L p^2 \mathrm{d}x$, p being the acoustic pressure. We want to express all these quantities in terms of the acoustic particle displacement, u. For T_a this is straightforward as $v = \mathrm{i}\omega u$ and for U_a we know from the continuity equation that $p = -\rho_0 c_0^2 \partial_x u$. The Lagrangian for the fluid is then given by,

$$\mathcal{L}_a = T_a - U_a + W_{ra} = \frac{1}{2}\omega^2 \int_0^L \rho_0 h u^2 \mathrm{d}x - \frac{1}{2}\int_0^L \rho_0 c_0^2 h \left(\partial_x u\right)^2 \mathrm{d}x + u(L)\frac{f_r}{h}, \tag{1}$$

where f_r/h is the force per unit length done by the resonator on the fluid. Note that we could also have directly obtained U_a from the integral of the product of the strain $\partial_x u$ and the stress $\rho_0 c_0^2 \partial_x u$.

The Lagrangian of the resonator is given by subtracting the potential energy, U_r, from the kinetic one, T_r, and adding the work done by the acoustic pressure on the resonator, W_{ar},

$$\mathcal{L}_r = T_r - U_r + W_{ar} = \frac{1}{2}\omega^2 m w_r^2 - \frac{1}{2}k w_r^2 - w_r h p(L), \tag{2}$$

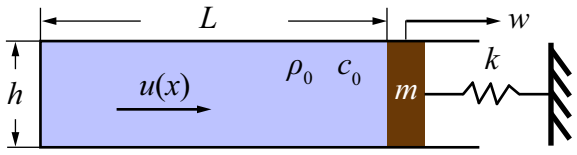

Figure 1: Schematic of the 1D problem consisting of acoustic plane waves in a duct coupled to a resonator.

where w_r is the resonator displacement.

From Eqs. (1) and (2), we can compute the Lagrangian of the total system as,

$$\begin{aligned}\mathcal{L} &= \mathcal{L}_a + \mathcal{L}_r = T_a + T_r - U_a - U_r + W_{ra} + W_{ar} = T_a + T_r - U_a - U_r \\ &= \frac{1}{2}\omega^2 \int_0^L \rho_0 h u^2 \mathrm{d}x + \frac{1}{2}\omega^2 m w_r^2 - \frac{1}{2}\int_0^L \rho_0 c_0^2 h \left(\partial_x u\right)^2 \mathrm{d}x - \frac{1}{2} k w_r^2,\end{aligned} \tag{3}$$

since $W_{ra} = -W_{ar}$, that is, the work done by the resonator on the fluid must be the negative of that done by the acoustic pressure on the resonator. Considering that the transmission conditions at the fluid-structure interface involve the continuity of displacements and tractions, i.e, $u(L) = w_r$ and $f_r/h = hp(L)$, if the former is satisfied then the compensation of internal work implies $w_r\left[f_r/h - hp(L)\right] = 0$. In other words, continuity of traction is automatically fulfilled in the Lagrangian (in a weak sense), while the continuity of displacements must be imposed in a strong sense when deriving the problem solution. This will be made clearer in the following and when addressing the 2D and 3D cases.

2.3. Discretization of the 1D system using the Rayleigh-Ritz method with Gaussian functions

Let us next proceed to find the discrete equation of motion of the problem using the Rayleigh-Ritz method. We expand the acoustic particle displacement $u(x)$ as a combination of basis functions $\partial_x\varphi_i(x)$ with coefficients A_i, such that

$$u(x) = \sum_{i=1}^{n} \partial_x\varphi_i(x) A_i =: \partial_x\boldsymbol{\varphi}^\top(x)\boldsymbol{A}. \tag{4}$$

Here, $\partial_x\varphi_i(x)$ are first-order derivatives of Gaussian functions $\varphi_i(x) = \exp\left[-(2^r x - s_i)^2/2\right]$, where r represents the scaling parameter and s_i the i-th translation one (see the works on the Gaussian expansion method (GEM) in [68–70] for details). The reason for choosing the derivatives of Gaussian functions instead of the Gaussians themselves is explained in Remark 1 below.

Substituting Eq. (4) into Eq. (3) we get the approximated Lagrangian,

$$\begin{aligned}\mathcal{L} &\simeq \frac{1}{2}\omega^2 \boldsymbol{A}^\top \left(\int_0^L \rho_0 h \partial_x\boldsymbol{\varphi}\partial_x\boldsymbol{\varphi}^\top \mathrm{d}x\right)\boldsymbol{A} + \frac{1}{2}\omega^2 m w_r^2 - \frac{1}{2}\boldsymbol{A}^\top\left(\int_0^L \rho_0 c_0^2 h \partial_{xx}^2\boldsymbol{\varphi}\partial_{xx}^2\boldsymbol{\varphi}^\top \mathrm{d}x\right)\boldsymbol{A} - \frac{1}{2}k w_r^2 \\ &=: \frac{1}{2}\omega^2\boldsymbol{A}^\top\boldsymbol{M}_a\boldsymbol{A} + \frac{1}{2}\omega^2 m w_r^2 - \frac{1}{2}\boldsymbol{A}^\top\boldsymbol{K}_a\boldsymbol{A} - \frac{1}{2}k w_r^2, \\ &=: \frac{1}{2}\omega^2\boldsymbol{C}^\top\boldsymbol{M}\boldsymbol{C} - \frac{1}{2}\boldsymbol{C}^\top\boldsymbol{K}\boldsymbol{C},\end{aligned} \tag{5}$$

where in the second line we have introduced the mass and stiffness matrices $\boldsymbol{M}_a$ and $\boldsymbol{K}_a$, respectively, and in the third one we have defined $\boldsymbol{C} = [\boldsymbol{A}^\top, w_r]^\top$, $\boldsymbol{M} = \mathrm{diag}(\boldsymbol{M}_a, m)$ and $\boldsymbol{K} = \mathrm{diag}(\boldsymbol{K}_a, k)$.

From the Euler-Lagrange equation, $-\partial_{\boldsymbol{C}^\top}\mathcal{L} = \boldsymbol{0}$, we obtain the eigenvalue system

$$\left(\boldsymbol{K} - \omega^2\boldsymbol{M}\right)\boldsymbol{C} = \boldsymbol{0}. \tag{6}$$

Note at this point that, according to the definitions of $\boldsymbol{M}$ and $\boldsymbol{K}$ above, the acoustic displacement and the resonator displacement remain uncoupled in Eq. (6), even though the continuity of the traction at the interface is guaranteed by the way the matrices have been constructed.

To properly formulate the problem and obtain the fully coupled motion of the system, we must next impose the essential boundary conditions, namely the rigid condition at the left end of the duct and the continuity of displacements at the interface, i.e.,

$$u(0) = \partial_x\boldsymbol{\varphi}^\top(0)\boldsymbol{A} = 0, \tag{7}$$

$$u(L) = \partial_x\boldsymbol{\varphi}^\top(L)\boldsymbol{A} = w_r, \tag{8}$$

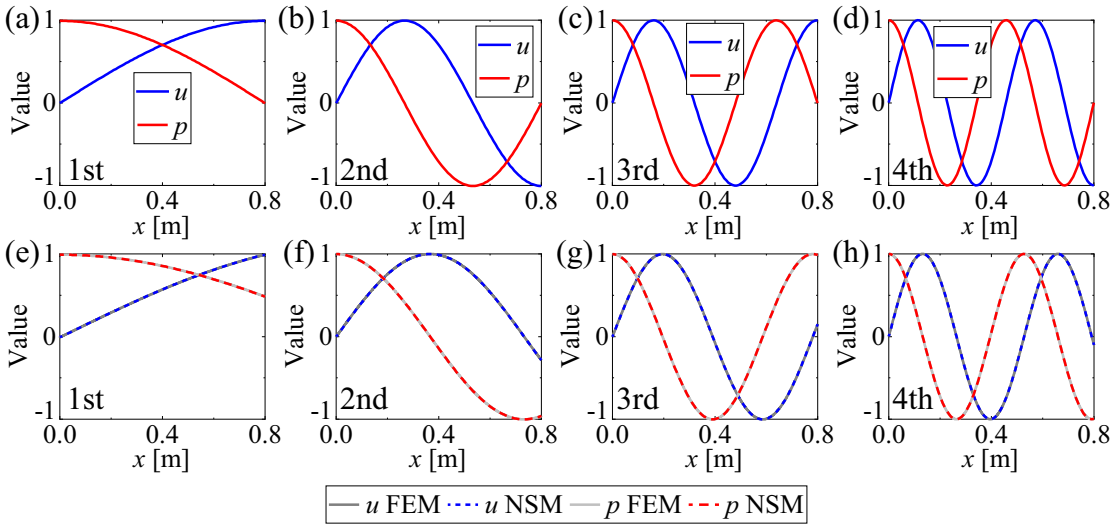

Figure 2: (a)-(d) The first 4 modal shapes for the uncoupled acoustic field. (e)-(h) The first 4 modal shapes of the acoustic field coupled to the resonator with the proposed method (NSM), together with the comparison with the FEM results. Here, both the acoustic pressure p and particle displacement u have been normalized with respect to their maximum values.

which can be rewritten as,

$$\begin{bmatrix} \partial_x \boldsymbol{\varphi}^\top(0) & 0 \\ \partial_x \boldsymbol{\varphi}^\top(L) & -1 \end{bmatrix} \begin{bmatrix} \boldsymbol{A} \\ w_r \end{bmatrix} =: \boldsymbol{\Phi}^\top \boldsymbol{C} = 0. \tag{9}$$

In the last equality we have introduced the constraint matrix $\boldsymbol{\Phi}^\top$. Following [44] we find a basis, say $\boldsymbol{Z}$, for the nullspace $\mathcal{N}(\boldsymbol{\Phi}^\top)$, and expand $\boldsymbol{C}$ as a linear combination of this basis, i.e., $\boldsymbol{C} = \boldsymbol{Z}\boldsymbol{\varepsilon}$, where $\boldsymbol{\varepsilon}$ is the coefficient column vector. Substituting this expression into Eq. (6) and pre-multiplying with $\boldsymbol{Z}^\top$ we get,

$$\left(\overline{\boldsymbol{K}} - \omega^2 \overline{\boldsymbol{M}}\right) \boldsymbol{\varepsilon} = \boldsymbol{0}, \tag{10}$$

where $\overline{\boldsymbol{K}} = \boldsymbol{Z}^\top \boldsymbol{K} \boldsymbol{Z}$ and $\overline{\boldsymbol{M}} = \boldsymbol{Z}^\top \boldsymbol{M} \boldsymbol{Z}$ are the new mass and stiffness matrices.

In Eq. (10), traction continuity is satisfied in a weak sense at the interface by the way in which the mass and stiffness matrices, $\boldsymbol{M}$ and $\boldsymbol{K}$, have been constructed, while displacement continuity is satisfied by the way the mass and stiffness matrices, $\overline{\boldsymbol{M}}$ and $\overline{\boldsymbol{K}}$, have been built, using the nullspace method. At this stage, the acoustic field in the duct and the resonator motion are perfectly coupled. Solving the eigenvalue problem in Eq. (10) we can obtain the eigenpairs $(\omega_n, \boldsymbol{\varepsilon}_n)$ of the coupled system. The n-th modal shape of the duct is given by $u_n(x) = \partial_x \boldsymbol{\varphi}^\top(x) \boldsymbol{Z} \boldsymbol{\varepsilon}_n$.

Remark 1. *The choice of first-order derivatives of Gaussians as admissible functions to expand the acoustic displacement in Eq. (4) may seem odd at first glance. One could have used the Gaussians themselves directly for the displacement or for the velocity potential, ϕ, so that $u = -(\mathrm{i}/\omega)\partial_x \phi$. But these options lead to complicate eigenvalue problems in which the mass or stiffness matrices or the continuity conditions at the interface depend on the angular frequency ω. The expansion in terms of Gaussian derivatives in Eq. (4) ensures that this is not the case and yields the standard generalized eigenvalue problems in Eqs. (6) and (10).*

Remark 2. *The mass and stiffness matrices of the eigenproblem in Eq. (10), are symmetric, a property not shared by many elastoacoustic formulations, as mentioned in the Introduction. Symmetry reduces the computational memory requirements and can be exploited to speed up the computations.*

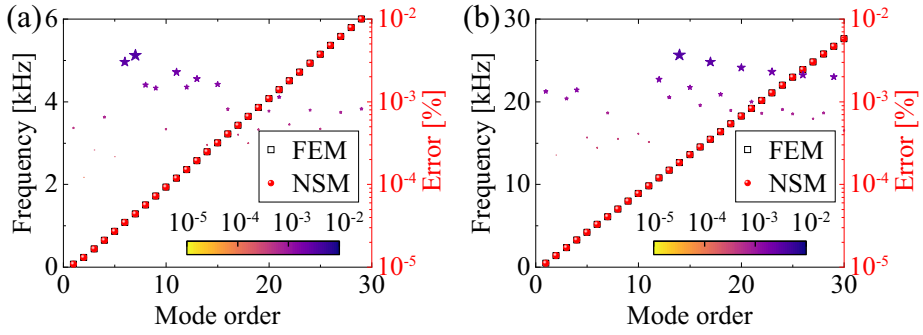

Figure 3: Comparison of the modal frequencies computed with NSM and FEM. (a) The fluid is air with density $\rho_0 = 1.21$ kg/m^3 and speed of sound $c_0 = 343$ m/s. (b) The fluid is water with $\rho_0 = 1000$ kg/m^3 and $c_0 = 1500$ m/s. The color and size of the stars indicate the relative percentage error between the NSM and FEM eigenfrequencies (see right axis and color bar).

2.4. Computation of the acoustic pressure field for the 1D system

While the above procedure allows us to obtain the acoustic particle displacement in the duct, in most problems the final variable of interest is the acoustic pressure. This can be calculated from the momentum conservation equation,

$$\partial_x p(x) = \rho_0 \omega^2 u(x), \tag{11}$$

so that

$$p(x) = \rho_0 \omega^2 \int u(x) \mathrm{d}x + C = \rho_0 \omega^2 \boldsymbol{\varphi}^\top(x) \boldsymbol{A} + C, \tag{12}$$

where C represents an unknown constant. The constant can be obtained by the strong imposition of the traction continuity at the interface, namely, $\left[f_r/h^2 - p(L)\right] = 0$. Since $p(x) = \rho_0 \omega^2 \boldsymbol{\varphi}^\top(x) \boldsymbol{A} + C$ and $f_r = -(k - \omega^2 m) w_r$, we get $C = (k - \omega^2 m) w_r / h^2 + \rho_0 \omega^2 \boldsymbol{\varphi}^\top(L) \boldsymbol{A}$.

Remark 3. *Alternatively, the acoustic pressure could be calculated from the mass conservation equation as* $p = -\rho_0 c_0^2 \partial_x u = -\rho_0 c_0^2 \partial_{xx}^2 \boldsymbol{\varphi}^\top(x) \boldsymbol{A}$. *However, this procedure involves the second derivative of Gaussians and produces less accurate results than Eq.* (12)*, which deals directly with the Gaussians themselves.*

2.5. Numerical simulations for the 1D system

Let us first present the results for the acoustic modes in the duct computed with Eq. (6), before the full coupling in Eq. (10). These are displayed in Figs. 2a-2d, where we show the normalized first 4 modal shapes for the acoustic particle displacement (blue lines) and the acoustic pressure (red lines). It is observed that $u(0) = 0$, indicating that the rigid condition is correctly imposed there. On the other hand, $u(L)$ reaches the maximum value and has zero slope at $x = L$, i.e., $\partial_x u(L) = 0$, showing that the strain is zero and therefore $p(L) = 0$, which corresponds to an open boundary. Therefore, the modes simply correspond to those of a rigid-open duct, which have analytical expressions $u_n(x) = \sin\left[\frac{\pi x(2n-1)}{2L}\right]$ $(n = 1, 2, 3, ...)$.

When we consider the full coupling between the duct and the piston using Eq. (10), the first 4 modal shapes present significant differences compared to the uncoupled ones, as observed in Figs. 2e-2h, where the results of a reference FEM model (built with the commercial software Comsol Multiphysics 6.2) have also been included for validation (gray lines). It is clear that for the first 3 modes $u(L)$ and $p(L)$ are strongly coupled to the resonator (compare Figs. 2e-2g with Figs. 2a-2c), while for the fourth mode $\partial_x p(L) \sim 0$ (see Fig. 2h), indicating that the piston essentially behaves as a rigid wall for the acoustic pressure. From the figure, it is noteworthy that the results of the proposed Rayleigh-Ritz approach using the NSM are fully consistent with those of the FEM (blue and red dashed lines versus gray ones), confirming its accuracy.

Table 1: Comparison of modal frequencies obtained using Gaussians as basis functions, different sets of sines and the FEM.

Order	FEM	102 Gaussians	100 Sines	200 Sines	300 Sines	500 Sines	1000 Sines
1	72.1	72.1	72.1	72.1	72.1	72.1	72.1
2	234.0	234.0	234.4	234.2	234.1	234.1	234.0
3	439.1	439.1	439.9	439.5	439.4	439.2	439.2
4	650.1	650.1	651.4	650.7	650.5	650.3	650.2
5	862.7	862.7	864.5	863.6	863.3	863.1	862.9
6	1076.1	1076.1	1078.2	1077.1	1076.8	1076.5	1076.3
7	1289.7	1289.7	1292.3	1291.0	1290.6	1290.3	1290.0
8	1503.6	1503.6	1506.7	1505.1	1504.6	1504.2	1503.9
9	1717.6	1717.6	1721.1	1719.4	1718.8	1718.3	1718.0
10	1931.7	1931.7	1935.6	1933.7	1933.0	1932.5	1932.1
11	2145.9	2145.9	2150.2	2148.0	2147.3	2146.7	2146.3
12	2360.0	2360.0	2364.8	2362.4	2361.6	2361.0	2360.5
13	2574.3	2574.3	2579.5	2576.9	2576.0	2575.3	2574.8
14	2788.5	2788.5	2794.2	2791.3	2790.4	2789.6	2789.1
15	3002.8	3002.8	3008.9	3005.8	3004.8	3004.0	3003.4
16	3217.0	3217.0	3223.6	3220.3	3219.2	3218.3	3217.7
17	3431.3	3431.3	3438.3	3434.8	3433.6	3432.7	3432.0
18	3645.6	3645.6	3653.0	3649.3	3648.1	3647.1	3646.3
19	3859.9	3859.9	3867.8	3863.8	3862.5	3861.5	3860.7
20	4074.2	4074.2	4082.5	4078.4	4077.0	4075.9	4075.1
21	4288.6	4288.6	4297.3	4292.9	4291.4	4290.3	4289.4
22	4502.9	4502.9	4512.1	4507.4	4505.9	4504.7	4503.8
23	4717.2	4717.2	4726.9	4722.0	4720.4	4719.1	4718.2
24	4931.5	4931.5	4941.6	4936.5	4934.9	4933.5	4932.5
25	5145.9	5145.9	5156.4	5151.1	5149.4	5148.0	5146.9
26	5360.2	5360.2	5371.2	5365.7	5363.8	5362.4	5361.3
27	5574.6	5574.6	5586.0	5580.2	5578.3	5576.8	5575.7
28	5788.9	5788.9	5800.8	5794.8	5792.8	5791.3	5790.1
29	6003.3	6003.3	6015.6	6009.4	6007.3	6005.7	6004.5
30	6217.6	6217.6	6230.4	6223.9	6221.8	6220.1	6218.9

To further validate the suggested methodology, we have calculated the modal frequencies and compared them with FEM results in Fig. 3a, for the first 30 mode orders. The relative error, $\epsilon = \frac{|\omega_{\text{FEM}} - \omega_{\text{NSM}}|}{\omega_{\text{FEM}}} \times 100\%$, is also included in the figure and represented by colored stars whose size and color indicate its value (see the right axis in red). It can be seen that $\epsilon < 0.01\%$ for the first 30 modal orders, demonstrating the precision of the Rayleigh-Ritz plus NSM method. The results in Fig. 3a correspond to the coupled system with the duct filled with air, as presented at the beginning of section 2. One may also wonder about how the method would perform for a heavy fluid like water, with $\rho_0 = 1000$ kg/m^3 and $c_0 = 1500$ m/s. As illustrated in Fig. 3b, the results again agree very well with the FEM ones, the relative error not exceedeing 0.01%.

Finally, and as mentioned above, the modal shapes for the acoustic field before coupling to the piston are sinusoids of the type, $u_n(x) = \sin\left[\frac{\pi x(2n-1)}{2L}\right]$ $(n = 1, 2, 3, ...)$. One could consider using them directly in Eq. (4) and Eq. (12) instead of Gaussians. In Table 1, we have listed the results of such a choice. In particular, the first 30 modal frequencies of the coupled system calculated respectively with the FEM, Rayleigh-Ritz plus NSM and 102 Gaussians, and Rayleigh-Ritz plus NSM using a number of sinusoids ranging from 100 to 1000 are presented. As can be seen, with the sole use of 102 Gaussians we can recover almost perfectly the modal frequencies of the FEM (note that in Table 1 we have only considered one decimal place so the first two columns look almost identical). In contrast, there are significant differences for the sinusoids. Although the results converge to the FEM and Gaussian ones as the number of sinusoids increases, they

are still unsatisfactory even for 1000 sinusoids. This demonstrates the advantage of using Gaussians as trial functions instead of sinusoids.

3. Two-dimensional (2D) problem

3.1. 2D problem description

In this section, we will see how the methodology for the 1D case can be generalized to 2D problems as an intermediate step before tackling a full 3D case. For this purpose, we consider a 2D rectangular cavity with rigid walls except for a flexible beam at the upper boundary, see Fig. 4. The cavity has length $L_x = 0.8$ m, width $L_y = 0.6$ m and it is filled with air of density $\rho_0 = 343$ kg/m^3 and sound speed $c_0 = 343$ m/s. The variables $u(x, y)$ and $v(x, y)$ now represent the particle displacements in the x and y directions, respectively, so that $\boldsymbol{u} = [u, v]^\top$. As for the beam, it has thickness $h = 0.005$ m and it is made of steel, with Young modulus $E = 210$ GPa and density $\rho = 7800$ kg/m^3. Since it is very thin, only the bending motion, $w_b(x)$, is considered.

3.2. Lagrangian of the 2D system

The Lagrangian of the acoustic field inside the cavity is given by the difference between its acoustic kinetic energy, T_a, and the potential one, U_a, plus the work done by the beam on the fluid, W_{ba}, namely,

$$\mathcal{L}_a = T_a - U_a + W_{ba} = \frac{1}{2}\omega^2 \int_0^{L_y}\int_0^{L_x} \rho_0(u^2 + v^2)\mathrm{d}x\mathrm{d}y - \frac{1}{2}\int_0^{L_y}\int_0^{L_x} \rho_0 c_0^2 \left(\partial_x u + \partial_y v\right)^2 \mathrm{d}x\mathrm{d}y + \frac{1}{L_x^2}\int_0^{L_x} v f_b \,\mathrm{d}x, \tag{13}$$

where f_b is the force exerted by the beam on the fluid. The Lagrangian of the beam is

$$\mathcal{L}_b = T_b - U_b + W_{ab} = \frac{1}{2}\omega^2 \int_0^{L_x} \rho h w_b^2 \mathrm{d}x - \frac{1}{2}\int_0^{L_x} EI \left(\partial_{xx}^2 w_b\right)^2 \mathrm{d}x + \int_0^{L_x} w_b p \,\mathrm{d}x, \tag{14}$$

with p the pressure exerted by the fluid on the beam. E and $I = h^3/12$ are the Young modulus and the moment of inertia, respectively. Since there is no additional term in the Lagrangian due to natural boundary conditions at the endpoints, this means that we consider $\partial_{xx}^2 w_b(0) = \partial_{xx}^2 w_b(L_x) = 0$, i.e., the bending momentum there is zero. On the other hand, and as for the 1D case, the internal work must compensate, $W_{ab} = -W_{ba}$, which guarantees traction continuity across the interface boundary in a weak sense. The Lagrangian of the entire 2D system is therefore given by,

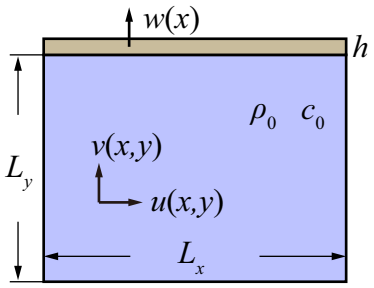

Figure 4: Schematic of the 2D system consisting of a cavity coupled to a flexible beam at its upper boundary.

$$\mathcal{L} = \mathcal{L}_a + \mathcal{L}_b = T_a + T_b - U_a - U_b = \frac{1}{2}\omega^2 \int_0^{L_y}\int_0^{L_x} \rho_0 (u^2 + v^2) \mathrm{d}x\mathrm{d}y + \frac{1}{2}\omega^2 \int_0^{L_x} \rho h w_b^2 \mathrm{d}x$$
$$- \frac{1}{2}\int_0^{L_y}\int_0^{L_x} \rho_0 c_0^2 \left(\partial_x u + \partial_y v\right)^2 \mathrm{d}x\mathrm{d}y - \frac{1}{2}\int_0^{L_x} EI \left(\partial_{xx}^2 w_b\right)^2 \mathrm{d}x. \quad (15)$$

3.3. Discretization of the 2D system using the Rayleigh-Ritz method with Gaussian functions

To discretize the 2D problem, we now expand each component of the acoustic displacement field in terms of first-order derivatives of 2D Gaussian functions,

$$u(x,y) = \partial_x \boldsymbol{\varphi}^\top(x,y)\boldsymbol{A}, \quad v(x,y) = \partial_y \boldsymbol{\varphi}^\top(x,y)\boldsymbol{A}, \quad (16)$$

where $\boldsymbol{\varphi}(x,y) = \boldsymbol{\alpha}(x) \otimes \boldsymbol{\beta}(y)$, with $\boldsymbol{\alpha}(x)$ and $\boldsymbol{\beta}(y)$ standing for 1D Gaussians in the x and y directions, respectively, and $\otimes$ represents Kronecker's product. This option guarantees irrotational flow, see Remark 4 below.

As for the beam displacement, $w_b(x)$, we directly express it in terms of 1D Gaussians, $\boldsymbol{\chi}(x)$ (see [68]),

$$w_b(x) = \boldsymbol{\chi}^\top(x)\boldsymbol{B}, \quad (17)$$

with $\boldsymbol{B}$ being the vector of coefficients.

Introducing Eq. (16) and Eq. (17) into Eq. (15) results in the approximated Lagrangian,

$$\begin{aligned}
\mathcal{L} \simeq\ & \frac{1}{2}\omega^2 \boldsymbol{A}^\top \left[\int_0^{L_y}\int_0^{L_x} \rho_0 \left(\partial_x\boldsymbol{\varphi}\partial_x\boldsymbol{\varphi}^\top + \partial_y\boldsymbol{\varphi}\partial_y\boldsymbol{\varphi}^\top\right)\mathrm{d}x\mathrm{d}y\right]\boldsymbol{A} + \frac{1}{2}\omega^2 \boldsymbol{B}^\top \left[\int_0^{L_x} \rho h \boldsymbol{\chi}\boldsymbol{\chi}^\top \mathrm{d}x\right]\boldsymbol{B} \\
& - \frac{1}{2}\boldsymbol{A}^\top \left[\int_0^{L_y}\int_0^{L_x} \rho_0 c_0^2 \left(\partial_{xx}^2\boldsymbol{\varphi}\partial_{xx}^2\boldsymbol{\varphi}^\top + \partial_{xx}^2\boldsymbol{\varphi}\partial_{yy}^2\boldsymbol{\varphi}^\top + \partial_{yy}^2\boldsymbol{\varphi}\partial_{xx}^2\boldsymbol{\varphi}^\top + \partial_{yy}^2\boldsymbol{\varphi}\partial_{yy}^2\boldsymbol{\varphi}^\top\right)\mathrm{d}x\mathrm{d}y\right]\boldsymbol{A} \\
& - \frac{1}{2}\boldsymbol{B}^\top \left[\int_0^{L_x} EI\partial_{xx}^2\boldsymbol{\chi}\partial_{xx}^2\boldsymbol{\chi}^\top \mathrm{d}x\right]\boldsymbol{B} \\
=:\ & \frac{1}{2}\omega^2 \boldsymbol{A}^\top \boldsymbol{M}_a \boldsymbol{A} + \frac{1}{2}\omega^2 \boldsymbol{B}^\top \boldsymbol{M}_b \boldsymbol{B} - \frac{1}{2}\boldsymbol{A}^\top \boldsymbol{K}_a \boldsymbol{A} - \frac{1}{2}\boldsymbol{B}^\top \boldsymbol{K}_b \boldsymbol{B}, \quad (18)
\end{aligned}$$

where in the last line we have introduced the fluid and beam mass matrices, $\boldsymbol{M}_a$ and $\boldsymbol{M}_b$, and the stiffness ones, $\boldsymbol{K}_a$ and $\boldsymbol{K}_b$. Applying the Euler-Lagrange equations to Eq. (18) yields the eigenvalue problem

$$\left(\begin{bmatrix} \boldsymbol{K}_a & \boldsymbol{0} \\ \boldsymbol{0} & \boldsymbol{K}_b \end{bmatrix} - \omega^2 \begin{bmatrix} \boldsymbol{M}_a & \boldsymbol{0} \\ \boldsymbol{0} & \boldsymbol{M}_b \end{bmatrix}\right)\begin{bmatrix} \boldsymbol{A} \\ \boldsymbol{B} \end{bmatrix} = \boldsymbol{0}, \quad (19)$$

which can be written compactly as

$$\left(\boldsymbol{K} - \omega^2 \boldsymbol{M}\right)\boldsymbol{C} = \boldsymbol{0}, \quad (20)$$

with $\boldsymbol{C} = [\boldsymbol{A}^\top, \boldsymbol{B}^\top]^\top$, $\boldsymbol{K} = \mathrm{diag}(\boldsymbol{K}_a, \boldsymbol{K}_b)$ and $\boldsymbol{M} = \mathrm{diag}(\boldsymbol{M}_a, \boldsymbol{M}_b)$.

Next, we must supplement Eq. (19) with the essential conditions at the boundaries and at the coupling interface. On the one hand, the left, right and bottom walls of the fluid cavity are rigid so that $u(0,y) = u(L_x,y) = v(x,0) = 0$. Moreover, the beam is simply supported on the cavity so that $w_b(0) = w_b(L_x) = 0$. On the other hand, displacement continuity at the interface implies $v(x,L_y) = w_b,\ \forall x \in [0, L_x]$.

The discretization of all these conditions according to Eq. (16) and Eq. (17) can be written in matrix form as,

$$\begin{bmatrix} \partial_x \boldsymbol{\varphi}^\top(0,y) & \mathbf{0} \\ \partial_x \boldsymbol{\varphi}^\top(L_x,y) & \mathbf{0} \\ \partial_y \boldsymbol{\varphi}^\top(x,0) & \mathbf{0} \\ \mathbf{0} & \boldsymbol{\chi}^\top(0) \\ \mathbf{0} & \boldsymbol{\chi}^\top(L_x) \\ \partial_y \boldsymbol{\varphi}^\top(x,L_y) & -\boldsymbol{\chi}^\top(x) \end{bmatrix} \begin{bmatrix} \boldsymbol{A} \\ \boldsymbol{B} \end{bmatrix} =: \boldsymbol{\Phi}^\top \boldsymbol{C} = \mathbf{0}. \tag{21}$$

The first three rows of the matrix in Eq. (21) correspond to the rigid boundaries of the cavity, the fourth and fifth to the no displacement condition at the end points of the beam, and the sixth row to the fluid and beam displacement continuity at the interface. In this case, however, instead of directly finding the nullspace of $\boldsymbol{\Phi}^\top$, we will work with a modification of it to avoid numerical instabilities. Let us denote the rows of $\boldsymbol{\Phi}^\top$ by $\boldsymbol{\Phi}_i$ with $i = 1 \dots 6$ and build the new matrix $\boldsymbol{\Psi}$ as,

$$\boldsymbol{\Psi} := \int_0^{L_y} \boldsymbol{\Phi}_1^\top \boldsymbol{\Phi}_1 \mathrm{d}y + \int_0^{L_y} \boldsymbol{\Phi}_2^\top \boldsymbol{\Phi}_2 \mathrm{d}y + \int_0^{L_x} \boldsymbol{\Phi}_3^\top \boldsymbol{\Phi}_3 \mathrm{d}x + \boldsymbol{\Phi}_4^\top \boldsymbol{\Phi}_4 + \boldsymbol{\Phi}_5^\top \boldsymbol{\Phi}_5 + \int_0^{L_x} \boldsymbol{\Phi}_6^\top \boldsymbol{\Phi}_6 \mathrm{d}x, \tag{22}$$

which by construction also satisfies $\boldsymbol{\Psi}\boldsymbol{C} = \mathbf{0}$. Next, we find a basis for the nullspace of $\boldsymbol{\Psi}$, say $\boldsymbol{Z}$, such that $\mathcal{N}(\boldsymbol{\Psi}) = \mathrm{span}\{\boldsymbol{Z}_i\}$, with $\boldsymbol{Z}_i$ being the columns of $\boldsymbol{Z}$, and then express $\boldsymbol{C}$ in Eq. (20) in terms of this basis, i.e., $\boldsymbol{C} = \boldsymbol{Z}\boldsymbol{\varepsilon}$. This gives the following eigenvalue problem that satisfies the natural, essential and coupling boundary conditions for the 2D system,

$$\left(\overline{\boldsymbol{K}} - \omega^2 \overline{\boldsymbol{M}}\right) \boldsymbol{\varepsilon} = \mathbf{0}, \tag{23}$$

with $\overline{\boldsymbol{K}} = \boldsymbol{Z}^\top \boldsymbol{K} \boldsymbol{Z}$ and $\overline{\boldsymbol{M}} = \boldsymbol{Z}^\top \boldsymbol{M} \boldsymbol{Z}$.

Remark 4. *Expanding u and v in terms of the derivatives of 2D Gaussian functions in Eq. (16) now has even more advantages than for the 1D case. Not only can we derive a standard generalized eigenvalue problem for the system, but also the irrotational flow condition is automatically satisfied by construction. That is, from Eq. (16) we observe that the displacement vector, $\boldsymbol{u}$, is nothing but the gradient of the scalar function $\boldsymbol{\varphi}^\top(x,y)\boldsymbol{A}$, i.e., $\boldsymbol{u} = (u,v) = \boldsymbol{\nabla}[\boldsymbol{\varphi}^\top(x,y)\boldsymbol{A}]$. Given that the rotational of a gradient is always zero, we have $\boldsymbol{\nabla} \times \boldsymbol{u} = \boldsymbol{\nabla} \times \boldsymbol{\nabla}[\boldsymbol{\varphi}^\top(x,y)\boldsymbol{A}] = \mathbf{0}$, so the flow is irrotational. This also applies to the 3D case analyzed in section 4. While natural in the current formulation, as mentioned in the Introduction this is a difficult problem for some displacement FEM implementations, where, for example, penalty methods are needed to impose the constraint of irrotational flow.*

3.4. Computation of the acoustic pressure field for the 2D system

Having computed the acoustic displacement field inside the cavity, $\boldsymbol{u}(x,y)$, for the coupled problem, we can also calculate the acoustic pressure field $p(x,y)$. To do so we resort to the displacement potential ϕ, such that $\boldsymbol{u} = \nabla\phi$. The equation of momentum conservation and the constitutive equation for the acoustic field can be written in terms of ϕ as (see [14]),

$$\nabla p = \rho_0 \omega^2 \nabla \phi, \tag{24a}$$

$$p = -\rho_0 c_0^2 \nabla^2 \phi, \tag{24b}$$

while the displacement at the boundary in terms of ϕ is given by,

$$\partial_y \phi(x, L_y) = v(x, L_y). \tag{25}$$

Integrating Eq. (24b) over the acoustic domain we obtain,

$$\int_0^{L_y}\int_0^{L_x} p\,\mathrm{d}x\mathrm{d}y = -\rho_0 c_0^2 \int_0^{L_x} v(x, L_y)\,\mathrm{d}x, \tag{26}$$

where we have applied the divergence theorem considering that $\partial_x\phi(0, y) = \partial_x\phi(L_x, y) = \partial_y\phi(x, 0) = 0$ and make use of Eq. (25). On the other hand, it follows from Eq. (24a) that

$$p = \rho_0\omega^2\phi + C, \tag{27}$$

with C being a constant. We can find its value by substituting Eq. (27) into Eq. (26), which yields,

$$C = -\frac{\rho_0\omega^2}{L_x L_y}\int_0^{L_y}\int_0^{L_x} \phi\ \mathrm{d}x\mathrm{d}y - \frac{\rho_0 c_0^2}{L_x L_y}\int_0^{L_x} v(x, L_y)\ \mathrm{d}x. \tag{28}$$

The last term represents the static pressure, i.e., the variation of pressure following a static deformation of the interface of amplitude v. It corresponds to the pressure at zero frequency ($\omega = 0$). From Eq. (27), the acoustic pressure is finally given by,

$$p = \rho_0\omega^2\left(\phi - \frac{1}{L_x L_y}\int_0^{L_y}\int_0^{L_x} \phi\ \mathrm{d}x\mathrm{d}y\right) - \frac{\rho_0 c_0^2}{L_x L_y}\int_0^{L_x} v(x, L_y)\ \mathrm{d}x, \tag{29}$$

It should be noted that the discrete counterpart of this expression is particularly easy to compute from Eq. (16), given that $\boldsymbol{u} = (u, v) = (\partial_x\boldsymbol{\varphi}^\top\boldsymbol{A}, \partial_y\boldsymbol{\varphi}^\top\boldsymbol{A}) = (\partial_x\phi, \partial_y\phi)$ with $\phi = \boldsymbol{\varphi}^\top\boldsymbol{A}$. We get,

$$p = \rho_0\omega^2\left(\boldsymbol{\varphi}^\top - \frac{1}{L_x L_y}\int_0^{L_y}\int_0^{L_x} \boldsymbol{\varphi}^\top\mathrm{d}x\mathrm{d}y\right)\boldsymbol{A} - \frac{\rho_0 c_0^2}{L_x L_y}\left(\int_0^{L_x} \partial_y\boldsymbol{\varphi}^\top(x, L_y)\mathrm{d}x\right)\boldsymbol{A}. \tag{30}$$

Remark 5. *As an alternative to Eq. (30), it would also be possible to find a new set of basis functions, say $\boldsymbol{\xi}$, and force them to satisfy the constraint $\left(\int_0^{L_y}\int_0^{L_x}\boldsymbol{\xi}^\top\mathrm{d}x\mathrm{d}y\right)\boldsymbol{A} = 0$, which will contribute to Eq. (22). With such basis functions the second summand in the first parenthesis of Eq. (30) will disappear.*

3.5. Numerical simulations for the 2D system

Let us first focus on the particle displacement field within the cavity when coupled to the beam. In Fig. 5, we show the results for the the second, fourth, tenth and thirtieth modal orders. The colormap stands for the normalized displacement amplitude, $\sqrt{u^2 + v^2}$, while the green arrows indicate the direction and amplitude of the particle motion. As observed, for the second and fourth orders (see Figs. 5a and 5b), the motion takes place mainly in the upper half of the cavity, especially near the coupling interface at $y = L_y = 0.6$ m. The bottom of the cavity remains almost still. This means that the coupling between the two subsystems is weak and that most of the vibration is localized in the beam. In contrast, for the tenth modal order in Fig. 5c, significant displacement variations within the cavity and at the interface with the beam are observed, corresponding to strong coupling. As for the thirtieth modal order in Fig. 5d, it presents a very regular pattern inside the cavity and it is in fact a blocked mode in which the beam behaves like a rigid wall. Therefore, the coupling is again very weak in this case.

In Fig. 6, we present the acoustic pressure distributions corresponding to the modal orders in Fig. 5. Contour lines have been included for a better inspection of the patterns. It can be seen in Figs. 6a and 6b that the pressure levels at the bottom part of the cavity are relevant there as opposed to the particle displacement. In Fig. 6c, corresponding to the strongly coupled tenth modal order, the maxima and minima are distributed within the cavity, while for the thirtieth modal order in Fig. 6d the regular pattern of a blocked mode, in which the interface boundary seems to be as rigid as the others, is observed.

Since one of the contributions of this paper concerns the way in which displacement continuity is imposed at the interface using the nullspace method, we next examine this issue in some detail. In Fig. 7 we have

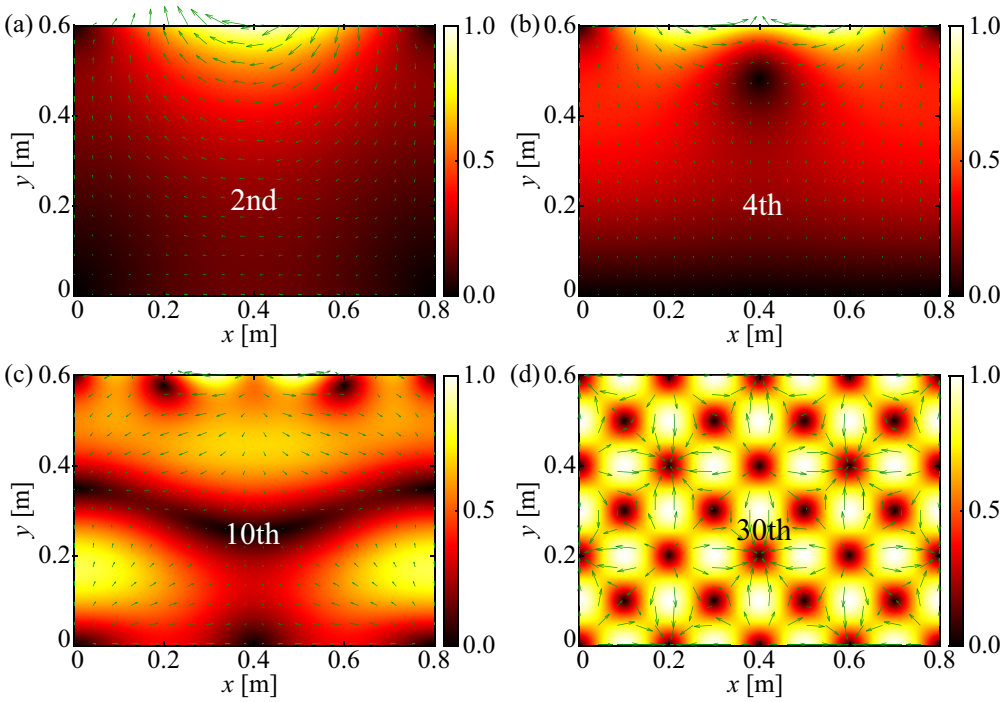

Figure 5: Magnitude $\sqrt{u^2+v^2}$ (normalized) and directions of the acoustic displacement in the 2D cavity coupled to the beam for the second (a), fourth (b), tenth (c) and thirtieth (d) modes.

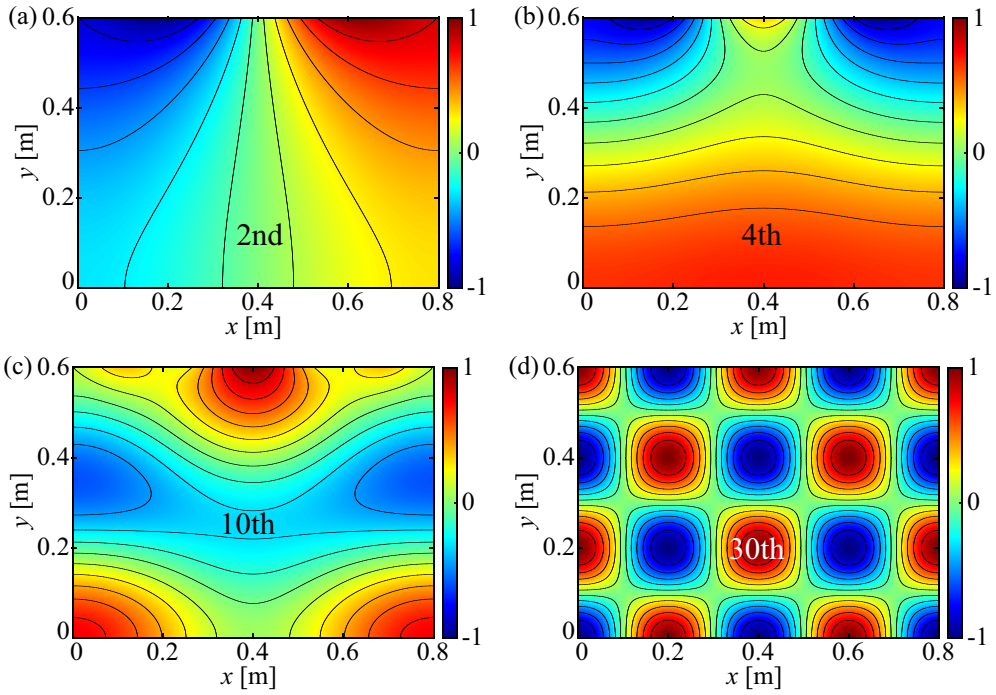

Figure 6: Acoustic modal pressure (normalized) in the 2D cavity coupled to the beam for the second (a), fourth (b), tenth (c) and thirtieth (d) modes.

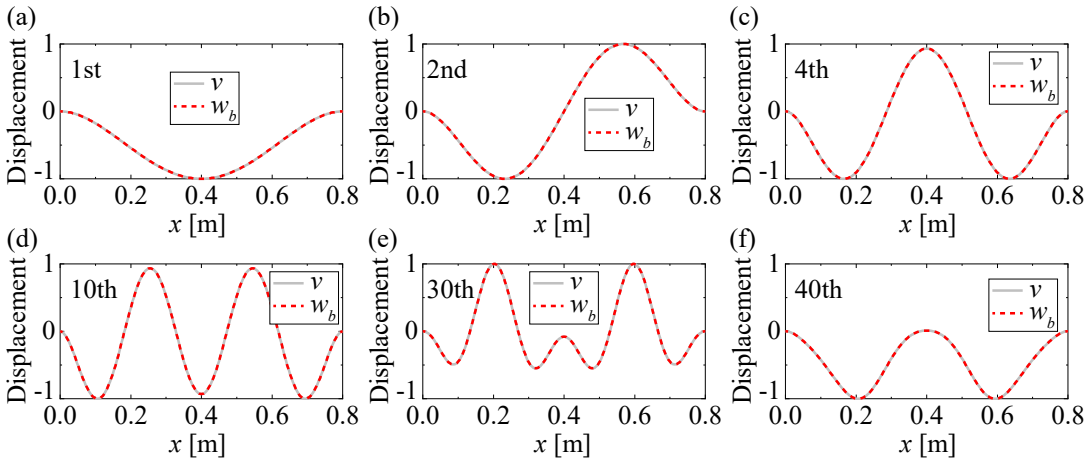

Figure 7: Comparison of the normal displacement of the cavity, $v(x, L_y)$, and of the beam, $w_b(x)$, at the interface for the first (a), second (b), fourth (c), tenth (d), thirtieth (e) and fortieth mode orders.

plotted the acoustic displacement $v(x, L_y)$ and the bending displacement of the beam $w_b(x)$ for different modal orders. It can be seen that both displacements are almost identical, showing that the imposition of displacement continuity by Eq. (22) yields very accurate results.

4. 3D problem description

Finally, to complete the work, we will present a 3D example consisting of a 3D cavity with rigid walls except for the upper one, where we have a flexible plate. A drawing of the system is shown in Fig. 8. The cavity has length $L_x = 0.8$ m, width $L_y = 0.6$ m and height $L_z = 0.5$ m. The particle displacements in the x, y, and z directions are respectively denoted as $u(x, y, z)$, $v(x, y, z)$ and $w(x, y, z)$. Again, the cavity is filled with air of density ρ_0=1.21 kg/m^3 and speed of sound $c_0 = 343$ m/s. As regards the plate, it has a thickness of $h = 0.005$ m and is placed at $z = L_z$. It is made of steel and, as in the 2D case, we will only consider the transverse displacement $w_p(x, y)$. Likewise, we assume that the plate is simply supported at its boundaries.

4.1. Lagrangian of the 3D system

Since the 3D case is very similar to the 2D case, and basically only the contribution of the z-component in the equations for the cavity and the y-component for the plate need to be added, we will not present all the mathematical developments as they are analogous to those in the previous sections (see also [69, 70] for further details).

The Lagrangian of the total 3D system, $\mathcal{L}$, is obtained as the summation of the cavity and plate Lagrangians, $\mathcal{L}_a$ and $\mathcal{L}_p$, and it is given by,

$$\begin{aligned}\mathcal{L} = \mathcal{L}_a + \mathcal{L}_p = &\frac{1}{2}\omega^2 \int_0^{L_z}\int_0^{L_y}\int_0^{L_x} \rho_0(u^2+v^2+w^2)\mathrm{d}x\mathrm{d}y\mathrm{d}z + \frac{1}{2}\omega^2 \int_0^{L_y}\int_0^{L_x} \rho h w_p^2 \mathrm{d}x\mathrm{d}y \\ &- \frac{1}{2}\int_0^{L_z}\int_0^{L_y}\int_0^{L_x} \rho_0 c_0^2 \left(\partial_x u + \partial_y v + \partial_z w\right)^2 \mathrm{d}x\mathrm{d}y\mathrm{d}z \\ &- \frac{1}{2}\int_0^{L_x}\int_0^{L_x} D\left[\left(\partial_{xx}^2 w_p\right)^2 + 2\nu\partial_{xx}^2 w_p \partial_{yy}^2 w_p + \left(\partial_{yy}^2 w_p\right)^2 + 2(1-\nu)\left(\partial_{xy}^2 w_p\right)^2\right]\mathrm{d}x\mathrm{d}y, \end{aligned} \tag{31}$$

where the bending stiffness is $D = Eh^3/12$ and the Poisson ratio is $\nu = 0.3$. As for the 2D case, the internal work done by the fluid on the plate and viceversa compensate each other and do not appear in the

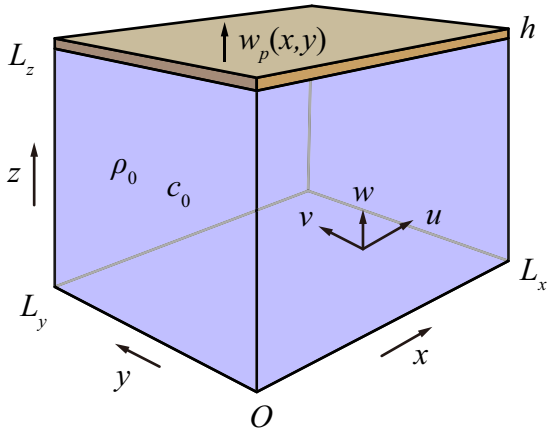

Figure 8: Schematic of the 3D system consisting of a volume cavity coupled to a flexible plate at its upper boundary.

Lagrangian, leading to the weak fulfillment of the continuity of traction at the interface. Also, no terms involving natural conditions appear in $\mathcal{L}_p$, which means that zero bending moment is assumed at the plate edges.

4.2. Discretization of the 3D system using the Rayleigh-Ritz method with Gaussian functions

The components of the acoustic displacement field are now discretized as,

$$u(x,y,z) = \partial_x \boldsymbol{\varphi}^\top(x,y,z)\boldsymbol{A}, \quad v(x,y,z) = \partial_y \boldsymbol{\varphi}^\top(x,y,z)\boldsymbol{A}, \quad w(x,y,z) = \partial_z \boldsymbol{\varphi}^\top(x,y,z)\boldsymbol{A}, \tag{32}$$

where $\boldsymbol{\varphi}(x,y,z) = \boldsymbol{\alpha}(x) \otimes \boldsymbol{\beta}(y) \otimes \boldsymbol{\gamma}(z)$ are 3D Gaussian functions and is $\boldsymbol{A}$ the coefficient vector. For the transverse displacement of the plate we take,

$$w_p(x,y) = \boldsymbol{\chi}^\top(x,y)\boldsymbol{B}, \tag{33}$$

with $\boldsymbol{\chi}(x,y) = \boldsymbol{\alpha}(x) \otimes \boldsymbol{\beta}(y)$ being 2D Gaussian functions and $\boldsymbol{B}$ the corresponding vector of coefficients. Substituting Eqs. (32) and (33) into Eq. (31) results in the approximated Lagrangian,

$$\begin{aligned}
\mathcal{L} \simeq\ & \frac{1}{2}\omega^2 \boldsymbol{A}^\top \left[\int_0^{L_z}\int_0^{L_y}\int_0^{L_x} \rho_0 \left(\partial_x\boldsymbol{\varphi}\partial_x\boldsymbol{\varphi}^\top + \partial_y\boldsymbol{\varphi}\partial_y\boldsymbol{\varphi}^\top + \partial_z\boldsymbol{\varphi}\partial_z\boldsymbol{\varphi}^\top \right) \mathrm{d}x\mathrm{d}y\mathrm{d}z \right] \boldsymbol{A} \\
& + \frac{1}{2}\omega^2 \boldsymbol{B}^\top \left[\int_0^{L_y}\int_0^{L_x} \rho h \boldsymbol{\chi}\boldsymbol{\chi}^\top \mathrm{d}x\mathrm{d}y \right] \boldsymbol{B} \\
& - \frac{1}{2}\boldsymbol{A}^\top \Bigg[\int_0^{L_z}\int_0^{L_y}\int_0^{L_x} \rho_0 c_0^2 \big(\partial^2_{xx}\boldsymbol{\varphi}\partial^2_{xx}\boldsymbol{\varphi}^\top + \partial^2_{yy}\boldsymbol{\varphi}\partial^2_{yy} + \partial^2_{zz}\boldsymbol{\varphi}\partial^2_{zz} + \partial^2_{xx}\boldsymbol{\varphi}\partial^2_{yy}\boldsymbol{\varphi}^\top + \partial^2_{yy}\boldsymbol{\varphi}\partial^2_{xx}\boldsymbol{\varphi}^\top \\
& + \partial^2_{xx}\boldsymbol{\varphi}\partial^2_{zz}\boldsymbol{\varphi}^\top + \partial^2_{zz}\boldsymbol{\varphi}\partial^2_{xx}\boldsymbol{\varphi}^\top + \partial^2_{yy}\boldsymbol{\varphi}\partial^2_{zz}\boldsymbol{\varphi}^\top + \partial^2_{zz}\boldsymbol{\varphi}\partial^2_{yy}\boldsymbol{\varphi}^\top \big) \mathrm{d}x\mathrm{d}y\mathrm{d}z \Bigg] \boldsymbol{A} \\
& - \frac{1}{2}\boldsymbol{B}^\top \Bigg[\int_0^{L_y}\int_0^{L_x} D\big(\partial^2_{xx}\boldsymbol{\chi}\partial^2_{xx}\boldsymbol{\chi}^\top + \nu\partial^2_{xx}\boldsymbol{\chi}\partial^2_{yy}\boldsymbol{\chi}^\top + \nu\partial^2_{yy}\boldsymbol{\chi}\partial^2_{xx}\boldsymbol{\chi}^\top + \partial^2_{yy}\boldsymbol{\chi}\partial^2_{yy}\boldsymbol{\chi}^\top \\
& + 2(1-\nu)\partial^2_{xy}\boldsymbol{\chi}\partial^2_{xy}\boldsymbol{\chi}^\top \big) \mathrm{d}x\mathrm{d}y \Bigg] \boldsymbol{B} \\
=:\ & \frac{1}{2}\omega^2 \boldsymbol{A}^\top \boldsymbol{M}_a \boldsymbol{A} + \frac{1}{2}\omega^2 \boldsymbol{B}^\top \boldsymbol{M}_p \boldsymbol{B} - \frac{1}{2}\boldsymbol{A}^\top \boldsymbol{K}_a \boldsymbol{A} - \frac{1}{2}\boldsymbol{B}^\top \boldsymbol{K}_p \boldsymbol{B},
\end{aligned} \tag{34}$$

where the mass, $\boldsymbol{M}_a$ and $\boldsymbol{M}_p$, and stiffness, $\boldsymbol{K}_a$ and $\boldsymbol{K}_p$, matrices for the fluid and plate have been defined in the last line. The Euler-Lagrange equations lead to the eigenvalue problem,

$$\left(\begin{bmatrix} \boldsymbol{K}_a & \boldsymbol{0} \\ \boldsymbol{0} & \boldsymbol{K}_p \end{bmatrix} - \omega^2 \begin{bmatrix} \boldsymbol{M}_a & \boldsymbol{0} \\ \boldsymbol{0} & \boldsymbol{M}_p \end{bmatrix} \right) \begin{bmatrix} \boldsymbol{A} \\ \boldsymbol{B} \end{bmatrix} = \boldsymbol{0}, \tag{35}$$

which is expressed in compact form as,

$$\left(\boldsymbol{K} - \omega^2 \boldsymbol{M} \right) \boldsymbol{C} = \boldsymbol{0}, \tag{36}$$

with $\boldsymbol{C} = [\boldsymbol{A}^\top, \boldsymbol{B}^\top]^\top$, $\boldsymbol{K} = \mathrm{diag}(\boldsymbol{K}_a, \boldsymbol{K}_p)$, and $\boldsymbol{M} = \mathrm{diag}(\boldsymbol{M}_a, \boldsymbol{M}_p)$.

Next we need to consider the essential boundary conditions of the problem. The walls of the cavity are rigid so that $u(0,y,z) = u(L_x,y,z) = v(x,0,z) = v(x,L_y,z) = w(x,y,0) = 0$. Given that the plate is simply supported we also have $w_p(x,0) = w_p(x,L_y) = w_p(0,y) = w_p(L_x,y) = 0$. Moreover, displacement continuity at the interface implies $w(x,y,L_z) = w_p(x,y)$. Discretizing these conditions and writing them in matrix form, we obtain

$$\begin{bmatrix} \partial_x \boldsymbol{\varphi}^\top(0,y,z) & \boldsymbol{0} \\ \partial_x \boldsymbol{\varphi}^\top(L_x,y,z) & \boldsymbol{0} \\ \partial_y \boldsymbol{\varphi}^\top(x,0,z) & \boldsymbol{0} \\ \partial_y \boldsymbol{\varphi}^\top(x,L_y,z) & \boldsymbol{0} \\ \partial_z \boldsymbol{\varphi}^\top(x,y,0) & \boldsymbol{0} \\ \boldsymbol{0} & \boldsymbol{\chi}^\top(x,0) \\ \boldsymbol{0} & \boldsymbol{\chi}^\top(x,L_y) \\ \boldsymbol{0} & \boldsymbol{\chi}^\top(0,y) \\ \boldsymbol{0} & \boldsymbol{\chi}^\top(L_x,y) \\ \partial_z \boldsymbol{\varphi}^\top(x,y,L_z) & -\boldsymbol{\chi}^\top(x,y) \end{bmatrix} \begin{bmatrix} \boldsymbol{A} \\ \boldsymbol{B} \end{bmatrix} =: \boldsymbol{\Phi}^\top \boldsymbol{C} = \boldsymbol{0}. \tag{37}$$

The first five rows of the matrix $\boldsymbol{\Phi}^\top$ correspond to the cavity rigid walls condition, while rows six to nine represent the zero displacement condition for the simply supported plate. The tenth row expresses the continuity of displacement at the interface. Following what was done in Eq. (22), we denote the rows of $\boldsymbol{\Phi}^\top$ by $\boldsymbol{\Phi}_i$, with $i = 1 \dots 10$, and introduce the new matrix $\boldsymbol{\Psi}$,

$$\begin{aligned} \boldsymbol{\Psi} := & \int_0^{L_z}\int_0^{L_y} \boldsymbol{\Phi}_1^\top \boldsymbol{\Phi}_1 \mathrm{d}y\mathrm{d}z + \int_0^{L_z}\int_0^{L_y} \boldsymbol{\Phi}_2^\top \boldsymbol{\Phi}_2 \mathrm{d}y\mathrm{d}z + \int_0^{L_z}\int_0^{L_x} \boldsymbol{\Phi}_2^\top \boldsymbol{\Phi}_2 \mathrm{d}x\mathrm{d}z + \int_0^{L_z}\int_0^{L_x} \boldsymbol{\Phi}_4^\top \boldsymbol{\Phi}_4 \mathrm{d}x\mathrm{d}z \\ & + \int_0^{L_y}\int_0^{L_x} \boldsymbol{\Phi}_5^\top \boldsymbol{\Phi}_5 \mathrm{d}x\mathrm{d}y + \int_0^{L_y} \boldsymbol{\Phi}_6^\top \boldsymbol{\Phi}_6 \mathrm{d}y + \int_0^{L_y} \boldsymbol{\Phi}_7^\top \boldsymbol{\Phi}_7 \mathrm{d}y + \int_0^{L_x} \boldsymbol{\Phi}_8^\top \boldsymbol{\Phi}_8 \mathrm{d}x + \int_0^{L_x} \boldsymbol{\Phi}_9^\top \boldsymbol{\Phi}_9 \mathrm{d}x \\ & + \int_0^{L_y}\int_0^{L_x} \boldsymbol{\Phi}_{10}^\top \boldsymbol{\Phi}_{10} \mathrm{d}x\mathrm{d}y, \end{aligned} \tag{38}$$

which satisfies $\boldsymbol{\Psi}\boldsymbol{C} = \boldsymbol{0}$. As for the 2D case, we next find a basis, $\boldsymbol{Z}$, for the nullspace of $\boldsymbol{\Psi}$, and span $\boldsymbol{C}$ in Eq. (36) in this basis, i.e., $\boldsymbol{C} = \boldsymbol{Z}\boldsymbol{\varepsilon}$. This yields the following eigenvalue problem satisfying all boundary conditions of the 3D system,

$$\left(\overline{\boldsymbol{K}} - \omega^2 \overline{\boldsymbol{M}} \right) \boldsymbol{\varepsilon} = \boldsymbol{0}, \tag{39}$$

with $\overline{\boldsymbol{K}} = \boldsymbol{Z}^\top \boldsymbol{K} \boldsymbol{Z}$ and $\overline{\boldsymbol{M}} = \boldsymbol{Z}^\top \boldsymbol{M} \boldsymbol{Z}$.

4.3. Computation of the acoustic pressure field for the 3D system

To compute the acoustic pressure within the 3D cavity we proceed identically to what was done in Section 3.4 for the 2D case, and resort to the displacement potential ϕ. The equivalent of Eq. (29) for the

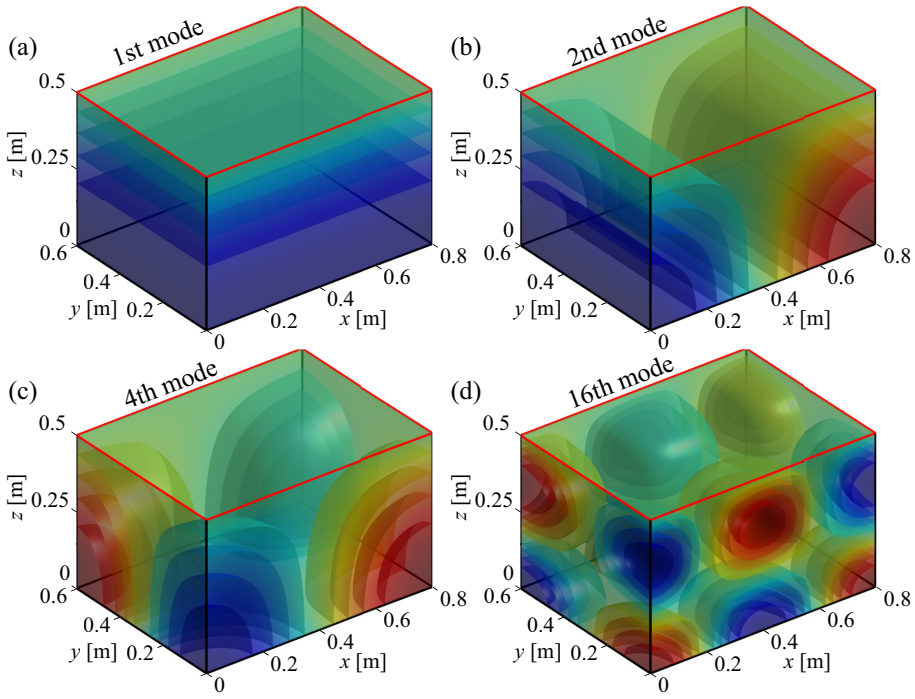

Figure 9: Sound pressure distribution in the 3D cavity for the first (a), second (b), fourth (c) and sixteenth (d) modal orders in the case of an pressure release upper boundary, i.e., $p(x, y, L_z) = 0$. In this and subsequent figures, the red frame represents the edges of the top surface of the cavity.

3D case is given by,

$$p = \rho_0\omega^2 \left(\phi - \frac{1}{L_x L_y L_z} \int_0^{L_z}\int_0^{L_y}\int_0^{L_x} \phi \, \mathrm{d}x\mathrm{d}y\mathrm{d}z \right) - \frac{\rho_0 c_0^2}{L_x L_y L_z} \int_0^{L_y}\int_0^{L_x} w(x, y, L_z) \, \mathrm{d}x\mathrm{d}y, \tag{40}$$

and its discrete counterpart (corresponding to Eq. (41) in the 2D case) reads,

$$p = \rho_0\omega^2 \left(\boldsymbol{\varphi}^\top - \frac{1}{L_x L_y L_z} \int_0^{L_z}\int_0^{L_y}\int_0^{L_x} \boldsymbol{\varphi}^\top \mathrm{d}x\mathrm{d}y \right) \boldsymbol{A} - \frac{\rho_0 c_0^2}{L_x L_y L_z} \left(\int_0^{L_y}\int_0^{L_x} \partial_z \boldsymbol{\varphi}^\top (x, y, L_z) \mathrm{d}x\mathrm{d}y \right) \boldsymbol{A}, \tag{41}$$

where we note again that the displacement potential is very easy to compute with the proposed formulation because $\boldsymbol{u} = (u, v, w) = (\partial_x \boldsymbol{\varphi}^\top \boldsymbol{A}, \partial_y \boldsymbol{\varphi}^\top \boldsymbol{A}, \partial_z \boldsymbol{\varphi}^\top \boldsymbol{A}) = (\partial_x \phi, \partial_y \phi, \partial_z \phi)$ with $\phi = \boldsymbol{\varphi}^\top \boldsymbol{A}$.

4.4. Numerical simulations for the 3D system

4.4.1. Cavity modes for open and rigid upper boundaries

Before presenting the results for the coupled cavity-plate problem, and to show the versatility of the proposed method in the 3D case, we first provide the acoustic cavity modes for different boundary conditions on the top surface. We start by assuming a pressure release boundary condition at $z = L_z$, i.e., $p(x, y, L_z) = 0$. To that goal, we modify Eq. (37) accordingly and compute the modes following the procedure in Section 4.2.

The pressure distribution for some modal orders is illustrated in Fig. 9. The first mode is longitudinal in the z direction, see Fig. 9a, while the second one is a transverse mode in the $x - z$ plane (Fig. 9b). The fourth and sixteenth modes are oblique and are presented in Figs. 9c and 9d, respectively. In all cases, the open condition on the upper boundary is satisfied, demonstrating the effectiveness of the NSM approach for this purpose.

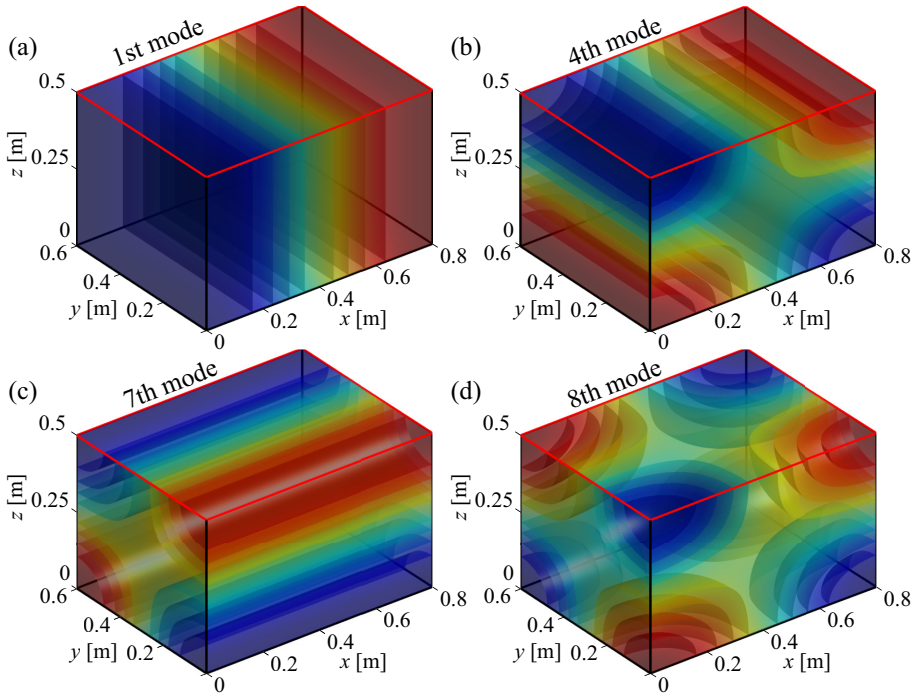

Figure 10: Sound pressure distribution in the 3D cavity for the first (a), fourth (b), seventh (c) and eight (d) modal orders in the case of a rigid upper boundary, i.e., $w_p(x, y, L_z) = 0$.

The method also works perfectly correctly if we impose a rigid boundary condition on the upper surface, i.e., $w(x, y, L_z) = 0$, as shown in Fig. 10 for various cavity modes. The first mode (see Fig. 10a) is a longitudinal mode in the x-direction, while in Figs. 10b and 10c, the fourth and seventh modes correspond to transverse modes in the $x - z$ and $y - z$ planes, respectively. In Fig. 10d, it can be seen that the eighth mode is an oblique one.

4.4.2. Coupled modes of the cavity-plate system

With regard to the coupling between the plate and the cavity, two different situations can be distinguished.

In the first one the plate dominates the vibration of the coupled system. Some modal orders for which this occurs are shown in Fig. 11. The acoustic displacement field is represented in the subfigures by cone-headed arrows whose color and length indicate the magnitude of the field. As can be seen, in all cases the largest displacements are near the top surface, with the motion at the bottom of the cavity being much smaller. In particular, the first, second, seventh and seventeenth modes are respectively shown in Figs. 11a, b, c and d. If we plot the corresponding plate displacement (see Figs. 12a, b, c and d) a clear pattern match is observed. For completeness, the modal pressure distribution within the cavity at these modes is plotted in Fig. 13, showing again that the strong variations occur mainly in the upper region of the cavity, driven by the plate motion.

In the second situation, the plate essentially acts as a rigid wall and the vibration field is dominated by the cavity. In Fig. 14, we have plotted the acoustic displacement field for the third, sixth, eleventh and nineteenth modes, again using cone-headed arrows to indicate the direction and magnitude of the point displacement. On the upper surface, all arrows are in the $x - y$ plane with negligible z component, as if the plate were rigid. The corresponding acoustic pressure distributions have been plotted Fig. 15. They correspond to classical blocked modes.

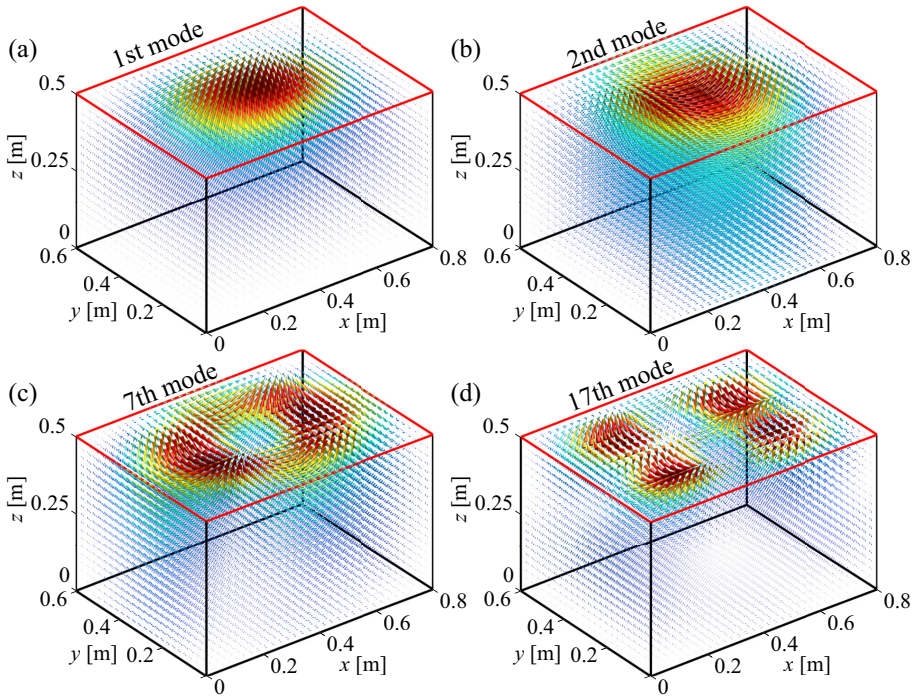

Figure 11: Acoustic displacement field in the 3D cavity coupled with the thin plate for the first (a), second (b), seventh (c) and seventeenth (d) modal orders. The direction of the arrows indicates those of the displacement field, while their color and length are proportional to their magnitude. The red frame at $z = 0.5$ m is the boundary of the plate.

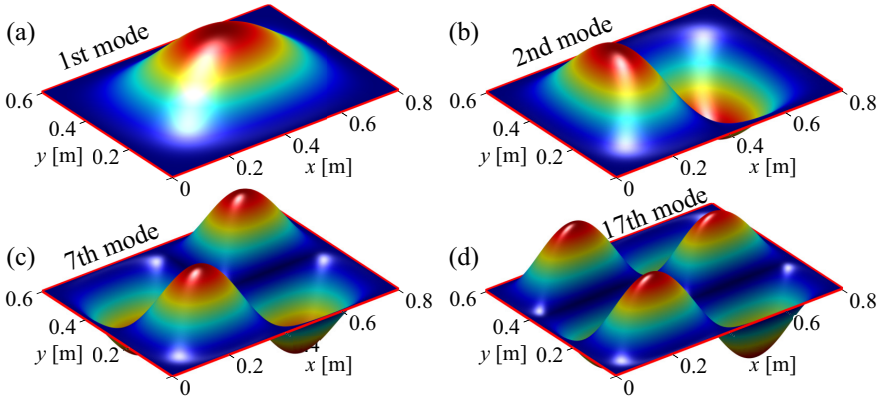

Figure 12: Modal vibration shapes of the plate coupled to the 3D cavity for the first (a), second (b), seventh (c) and seventeenth (d) modal orders.

5. Conclusions

In this paper we have proposed a displacement/acoustic displacement formulation to solve the two-way elastoacoustic problem. The formulation is established in the framework of the Rayleigh-Ritz method using Gaussians as basis functions. Compared to other approaches, it has some specificities in that it leads to a symmetric system without coupling matrices, the essential conditions being imposed on the boundaries, including the interface, by means of the nullspace method (NSM). Moreover, the irrotational nature of the acoustic field is implicitly guaranteed, since we expand the displacement components in terms of derivatives of Gaussians rather than Gaussians themselves, thus avoiding the appearance of spurious modes.

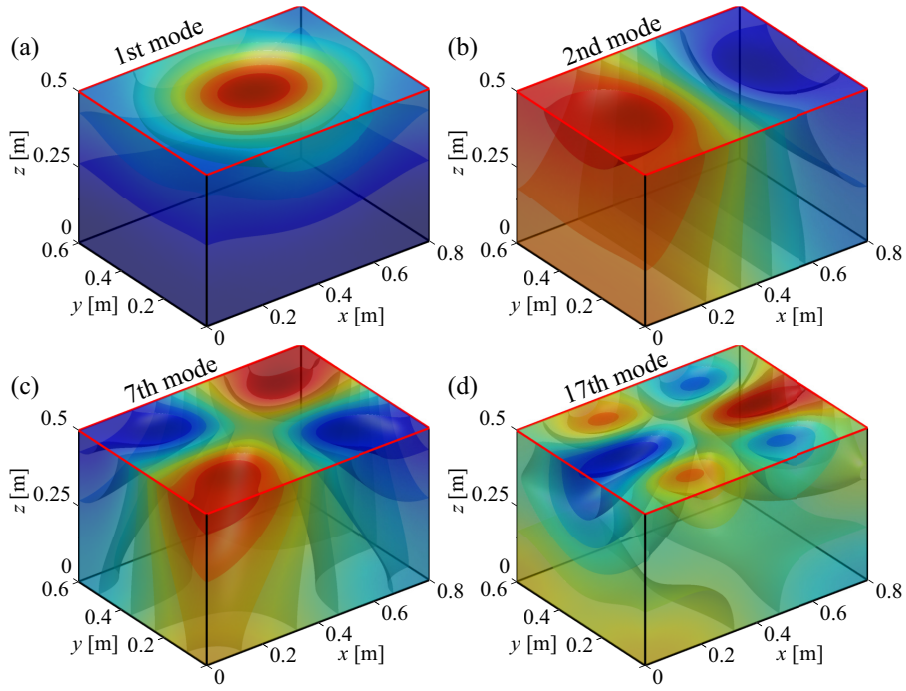

Figure 13: Sound pressure distribution in the 3D cavity coupled with the thin plate for the first (a), second (b), seventh (c) and seventeenth (d) modal orders.

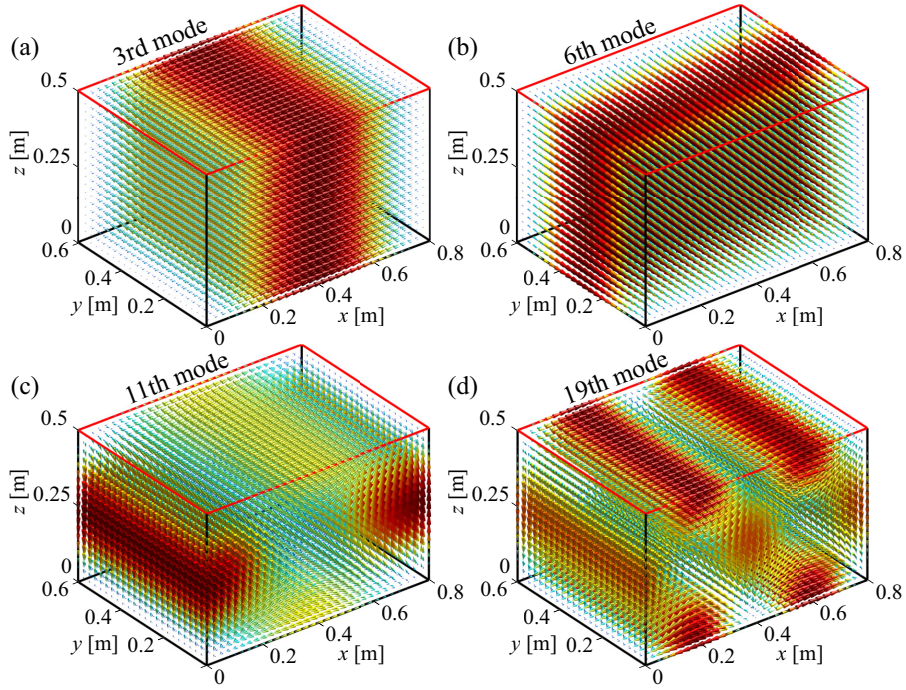

Figure 14: Acoustic displacement field in the 3D cavity coupled with the thin plate for the third (a), sixth (b), eleventh (c) and nineteenth (d) modal orders. The direction of the arrows indicates those of the displacement field, while their color and length are proportional to their magnitude. The red frame at $z = 0.5$ m is the boundary of the plate.

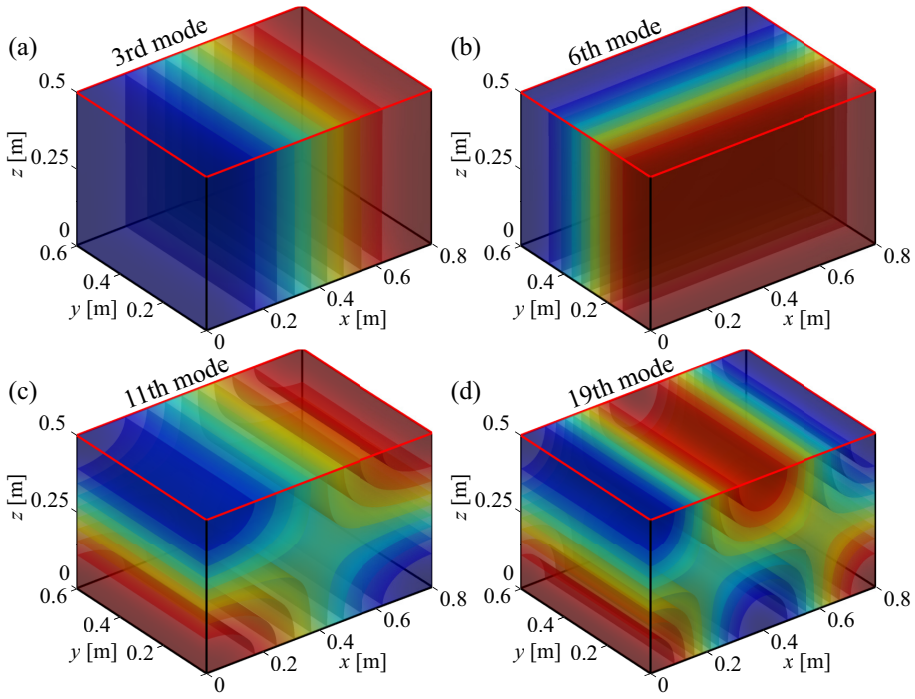

Figure 15: Sound pressure distribution in the 3D cavity coupled with the thin plate for the third (a), sixth (b), eleventh (c) and nineteenth (d) modal orders. In this case the plate behaves like a rigid wall and the modes can be identified as blocked modes.

To demonstrate the performance of the approach, we have first addressed a 1D problem consisting of sound waves propagating in a duct coupled to a resonator. The accuracy of the solution has been validated against finite element simulations by checking the modal shapes and frequencies. The maximum error is less than 0.01%, even for heavy fluids (water) instead of air. We have also demonstrated the advantage of using Gaussian rather than trigonometric basis functions in terms of the speed of convergence to the analytical solution. Next, the problem of the acoustic field in a 2D cavity coupled to a beam at its upper boundary has been considered. As said, the proposed approach guarantees the irrotationality of the flow for the 2D case and the NSM perfectly ensures the continuity of displacement at the interface (the continuity of traction is satisfied in a weak sense). Finally, we have extended the method to a 3D cavity coupled to a plate at its top boundary. It has been shown how the method can accurately deal with different types of boundary conditions and that for the coupled system one can distinguish between modes essentially driven by the motion of the plate and blocked modes in which the plate acts as if it were rigid. On the other hand, it is worth noting that when solving for structural and acoustic displacements, the variable of interest in the case of the cavity is usually the acoustic pressure. We have seen how this can be recovered once we have calculated the acoustic displacement using the displacement potential. Since we have expanded the acoustic displacement in terms of derivatives of Gaussians, the displacement potential is obtained directly in terms of Gaussians and is very easily incorporated into the proposed formulation. This allows us to obtain the acoustic pressure in a simple way.

Future work will consist of extending the approach to determine, for example, the acoustic transmission loss between cavities separated by a flexible plate. Also, the design of reduced order models (e.g., based on component mode synthesis) to recover the behavior of the coupled system in terms of the modal behaviour of its components (beam/plate plus cavity) will be addressed. Interestingly, the dissipation at the coupling interface could be somehow accounted for.

Acknowledgments

J. Deng acknowledges the support received by the National Natural Science Foundation of China (52301386), and the support of the Beatriu de Pinós postdoctoral program of the Department of Research and Universities of the Generalitat of Catalonia (2022 BP 00027). O. Guasch acknowledges the support of the Generalitat de Catalunya (Departament de Recerca i Universitats) through grant 2021 SGR 1396 awarded to the HER group. The authors would like to thank Prof. Ramon Codina, Polytechnic University of Catalonia (UPC), for his valuable comments and discussions on some of the contents of this article.

References

[1] A. Le Bot, Foundation of statistical energy analysis in vibroacoustics, OUP Oxford, 2015.
[2] L. G. Olson, K.-J. Bathe, Analysis of fluid-structure interactions. a direct symmetric coupled formulation based on the fluid velocity potential, Comput. Struct. 21 (1985) 21–32.
[3] J. B. Mariem, M. Hamdi, A new boundary finite element method for fluid–structure interaction problems, Int. J. Numer. Meth. Engrg. 24 (1987) 1251–1267.
[4] H. C. Chen, R. L. Taylor, Vibration analysis of fluid–solid systems using a finite element displacement formulation, Int. J. Numer. Meth. Engrg. 29 (1990) 683–698.
[5] A. Berry, J. Nicolas, Structural acoustics and vibration behavior of complex panels, Appl. Acoust. 43 (1994) 185–215.
[6] N. Atalla, R. Bernhard, Review of numerical solutions for low-frequency structural-acoustic problems, Appl. Acoust. 43 (1994) 271–294.
[7] F. J. Fahy, P. Gardonio, Sound and structural vibration: radiation, transmission and response, Elsevier, 2007.
[8] R. Ohayon, C. Soize, Computational vibroacoustics in low-and medium-frequency bands: damping, ROM, and UQ modeling, Appl. Sci. 7 (2017) 586.
[9] X. Wang, K. Bathe, Displacement/pressure based mixed finite element formulations for acoustic fluid–structure interaction problems, Int. J. Numer. Meth. Engrg. 40 (1997) 2001–2017.
[10] M. Petyt, Introduction to finite element vibration analysis, Cambridge university press, 2010.
[11] G. Everstine, A symmetric potential formulation for fluid-structure interaction, J. Sound Vib. 79 (1981) 157–160.
[12] M. Kaltenbacher, Numerical simulation of mechatronic sensors and actuators, volume 2, Springer, 2007.
[13] H. Morand, R. Ohayon, Substructure variational analysis of the vibrations of coupled fluid–structure systems. finite element results, Int. J. Numer. Meth. Engrg. 14 (1979) 741–755.
[14] H. J.-P. Morand, R. Ohayon, Fluid-structure interaction: Applied numerical methods, Wiley-Masson Series Research in Applied Mathematics, 1995.
[15] T. Belytschko, Fluid-structure interaction, Comput. Struct. 12 (1980) 459–469.
[16] M. A. Hamdi, Y. Ousset, G. Verchery, A displacement method for the analysis of vibrations of coupled fluid–structure systems, Int. J. Numer. Meth. Engrg. 13 (1978) 139–150.
[17] L. G. Olson, K.-J. Bathe, A study of displacement-based fluid finite elements for calculating frequencies of fluid and fluid-structure systems, Nucl. Eng. Des. 76 (1983) 137–151.
[18] A. Bermúdez, R. Rodríguez, Finite element computation of the vibration modes of a fluid—solid system, Comput. Methods Appl. Mech. Eng. 119 (1994) 355–370.
[19] A. Bermúdez, R. Durán, M. Muschietti, R. Rodríguez, J. Solomin, Finite element vibration analysis of fluid–solid systems without spurious modes, SIAM J. Numer. Anal. 32 (1995) 1280–1295.
[20] A. Bermúdez, L. Hervella-Nieto, R. Rodriguez, Finite element computation of three-dimensional elastoacoustic vibrations, J. Sound Vib. 219 (1999) 279–306.
[21] B. Flemisch, M. Kaltenbacher, S. Triebenbacher, B. I. Wohlmuth, The equivalence of standard and mixed finite element methods in applications to elasto-acoustic interaction, SIAM J. Sci. Comput. 32 (2010) 1980–2006.
[22] P. F. Antonietti, F. Bonaldi, I. Mazzieri, A high-order discontinuous Galerkin approach to the elasto-acoustic problem, Comput. Methods Appl. Mech. Eng. 358 (2020) 112634.
[23] P. F. Antonietti, M. Botti, I. Mazzieri, S. N. Poltri, A high-order discontinuous Galerkin method for the poro-elasto-acoustic problem on polygonal and polyhedral grids, SIAM J. Sci. Comput. 44 (2022) B1–B28.
[24] M. Muhr, B. Wohlmuth, V. Nikolić, A discontinuous Galerkin coupling for nonlinear elasto-acoustics, IMA J. Numer. Anal. 43 (2023) 225–257.
[25] M. Pirnat, G. Čepon, M. Boltežar, Structural–acoustic model of a rectangular plate–cavity system with an attached distributed mass and internal sound source: theory and experiment, J. Sound Vib. 333 (2014) 2003–2018.
[26] D. Shi, W. Ren, H. Zhang, G. Liu, Q. Wang, Vibro-acoustic coupling characteristics of orthotropic l-shaped plate–cavity coupling system, J. Low Freq. Noise Vib. Act. Control 39 (2020) 1102–1126.
[27] G. Wang, Z. Sheng, Y. Zhang, Z. Zhu, Q. Liu, J. Ni, Sound transmission characteristics of a plate backed by an irregular cavity, Mech. Syst. Signal Pr. 196 (2023) 110345.
[28] N. Atalla, J. Nicolas, C. Gauthier, Acoustic radiation of an unbaffled vibrating plate with general elastic boundary conditions, J. Acoust. Soc. Am. 99 (1996) 1484–1494.
[29] S. Wrona, M. Pawelczyk, J. Cheer, Acoustic radiation-based optimization of the placement of actuators for active control of noise transmitted through plates, Mech. Syst. Signal Pr. 147 (2021) 107009.

[30] S. N. Balireddy, J. Pitchaimani, L. B. Mailan Chinnapandi, V. Chintapalli, Acoustic response of an isotropic beam under axially variable loads using Ritz and Rayleigh integral methods, Arch. Acoust. 47 (2022).
[31] A. Berry, J.-L. Guyader, J. Nicolas, A general formulation for the sound radiation from rectangular, baffled plates with arbitrary boundary conditions, J. Acoust. Soc. Am. 88 (1990) 2792–2802.
[32] X. Zhang, W. L. Li, A unified approach for predicting sound radiation from baffled rectangular plates with arbitrary boundary conditions, J. Sound Vib. 329 (2010) 5307–5320.
[33] J. Legault, A. Mejdi, N. Atalla, Vibro-acoustic response of orthogonally stiffened panels: The effects of finite dimensions, J. Sound Vib. 330 (2011) 5928–5948.
[34] W. Zhang, L. Cui, R. Xu, Y. Peng, Fast analytical approximations for the acoustic radiation impedance of rectangular plates with arbitrary boundary conditions, AIP Adv. 13 (2023).
[35] H. Nélisse, O. Beslin, J. Nicolas, A generalized approach for the acoustic radiation from a baffled or unbaffled plate with arbitrary boundary conditions, immersed in a light or heavy fluid, J. Sound Vib. 211 (1998) 207–225.
[36] L. Ma, L. Cheng, Sound radiation and transonic boundaries of a plate with an acoustic black hole, J. Acoust. Soc. Am. 145 (2019) 164–172.
[37] L. Ma, L. Cheng, Topological optimization of damping layout for minimized sound radiation of an acoustic black hole plate, J. Sound Vib. 458 (2019) 349–364.
[38] L. Ma, L. Cheng, Numerical and experimental benchmark solutions on vibration and sound radiation of an acoustic black hole plate, Appl. Acoust. 163 (2020) 107223.
[39] J. Deng, O. Guasch, L. Maxit, L. Zheng, Annular acoustic black holes to reduce sound radiation from cylindrical shells, Mech. Syst. Signal Pr. 158 (2021) 107722.
[40] J. Deng, L. Zheng, Noise reduction via three types of acoustic black holes, Mech. Syst. Signal Pr. 165 (2022) 108323.
[41] J. Deng, O. Guasch, L. Maxit, N. Gao, Sound radiation and non-negative intensity of a metaplate consisting of an acoustic black hole plus local resonators, Compos. Struct. 304 (2023) 116423.
[42] J. Deng, N. Gao, X. Chen, H. Pu, J. Guo, Underwater sound radiation from a Mindlin plate with an acoustic black hole, Ocean Eng. 278 (2023) 114376.
[43] J. Deng, J. Ma, X. Chen, Y. Yang, N. Gao, J. Liu, Vibration damping by periodic additive acoustic black holes, J. Sound Vib. 574 (2024) 118235.
[44] J. Deng, Y. Xu, O. Guasch, N. Gao, L. Tang, Nullspace technique for imposing constraints in the Rayleigh—Ritz method, J. Sound Vib. 527 (2022) 116812.
[45] J. Deng, N. Gao, Broadband vibroacoustic reduction for a circular beam coupled with a curved acoustic black hole via nullspace method, Int. J. Mech. Sci. 233 (2022) 107641.
[46] J. Deng, O. Guasch, Sound waves in continuum models of periodic sonic black holes, Mech. Syst. Signal Pr. 205 (2023) 110853.
[47] J. Deng, Y. Xu, O. Guasch, N. Gao, L. Tang, W. Guo, A wave and Rayleigh–Ritz method to compute complex dispersion curves in periodic lossy acoustic black holes, J. Sound Vib. 546 (2023) 117449.
[48] J. Deng, Y. Xu, O. Guasch, N. Gao, L. Tang, X. Chen, A two-dimensional wave and rayleigh–ritz method for complex dispersion in periodic arrays of circular damped acoustic black holes, Mech. Syst. Signal Pr. 200 (2023) 110507.
[49] W. C. Hurty, Vibrations of structural systems by component mode synthesis, J. Eng. Mech. Div. 86 (1960) 51–69.
[50] W. C. Hurty, Dynamic analysis of structural systems using component modes, AIAA J. 3 (1965) 678–685.
[51] G. Gladwell, Branch mode analysis of vibrating systems, J. Sound Vib. 1 (1964) 41–59.
[52] R. J. Guyan, Reduction of stiffness and mass matrices, AIAA J. 3 (1965) 380–380.
[53] R. R. Craig Jr, M. C. Bampton, Coupling of substructures for dynamic analyses., AIAA J. 6 (1968) 1313–1319.
[54] C. Farhat, M. Géradin, On a component mode synthesis method and its application to incompatible substructures, Comput. Struct. 51 (1994) 459–473.
[55] J. Gerstmayr, J. Ambrósio, Component mode synthesis with constant mass and stiffness matrices applied to flexible multibody systems, Int. J. Numer. Meth. Engrg. 73 (2008) 1518–1546.
[56] U. L. Hetmaniuk, R. B. Lehoucq, A special finite element method based on component mode synthesis, ESAIM: Math. Model. Numer. Anal. 44 (2010) 401–420.
[57] C. Papadimitriou, D.-C. Papadioti, Component mode synthesis techniques for finite element model updating, Comput. Struct. 126 (2013) 15–28.
[58] J. Deng, O. Guasch, L. Maxit, N. Gao, An artificial spring component mode synthesis method for built-up structures, Int. J. Mech. Sci. 243 (2023) 108052.
[59] F. J. Fahy, Vibration of containing structures by sound in the contained fluid, J. Sound Vib. 10 (1969) 490–512.
[60] F. J. Fahy, Response of a cylinder to random sound in the contained fluid, J. Sound Vib. 13 (1970) 171–194.
[61] D. Karnopp, Coupled vibratory-system analysis, using the dual formulation, J. Acoust. Soc. Am. 40 (1966) 380–384.
[62] L. Maxit, J.-L. Guyader, Estimation of SEA coupling loss factors using a dual formulation and FEM modal information, part I: theory, J. Sound Vib. 239 (2001) 907–930.
[63] L. Maxit, J. L. Guyader, Extension of SEA model to subsystems with non-uniform modal energy distribution, J. Sound Vib. 265 (2003) 337–358.
[64] À. Aragonès, L. Maxit, O. Guasch, A graph theory approach to identify resonant and non-resonant transmission paths in statistical modal energy distribution analysis, J. Sound Vib. 350 (2015) 91–110.
[65] L. Maxit, O. Guasch, A dual modal formulation for multiple flexural subsystems connected at a junction in energy-based models, Mech. Syst. Signal Pr. 119 (2019) 457–470.
[66] L. Maxit, O. Guasch, Energy-based reformulated craig-bampton method for multiple flexural subsystems connected at a junction with low impedance mismatch, Mech. Syst. Signal Pr. 119 (2019) 471–485.

[67] M. Ouisse, L. Maxit, C. Cacciolati, J.-L. Guyader, Patch transfer functions as a tool to couple linear acoustic problems, J. Vib. Acoust. 127(5) (2005) 458–466.
[68] J. Deng, L. Zheng, P. Zeng, Y. Zuo, O. Guasch, Passive constrained viscoelastic layers to improve the efficiency of truncated acoustic black holes in beams, Mech. Syst. Signal Pr. 118 (2019) 461–476.
[69] J. Deng, L. Zheng, O. Guasch, H. Wu, P. Zeng, Y. Zuo, Gaussian expansion for the vibration analysis of plates with multiple acoustic black holes indentations, Mech. Syst. Signal Pr. 131 (2019) 317–334.
[70] J. Deng, O. Guasch, L. Zheng, Ring-shaped acoustic black holes for broadband vibration isolation in plates, J. Sound Vib. 458 (2019) 109–122.